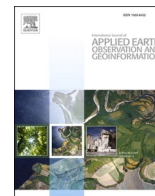Contents lists available at ScienceDirect

International Journal of Applied Earth Observation and Geoinformation

Characterization of ocean color retrievals and ocean diurnal variations using the Geostationary Ocean Color Imager (GOCI)

Menghua Wang [a,*], Wei Shi [a,b], Lide Jiang [a,b]

[a] *NOAA National Environmental Satellite, Data, and Information Service, Center for Satellite Applications and Research, 5830 University Research Ct., College Park, MD 20740, USA*
[b] *CIRA at Colorado State University, Fort Collins, CO, USA*

A B S T R A C T

Using measurements from the Geostationary Ocean Color Imager (GOCI) on the Communication, Ocean, and Meteorological Satellite (COMS), we characterize and quantify some advantages and applications of the satellite geostationary measurements, compared with those of the polar-orbiting satellites. With eight daily measurements in the western Pacific Ocean, the average GOCI daily coverage of ocean color retrievals reached ~43.81%, compared to ~21.77% from the Visible Infrared Imaging Radiometer Suite (VIIRS). The GOCI-measured ocean property data, such as normalized water-leaving radiance $[nL_w(\lambda)]$ and diffuse attenuation coefficient at 490 nm $[K_d(490)]$, show significant diurnal variability over the region, particularly over highly turbid coastal regions. It is noted that GOCI-derived $nL_w(\lambda)$ spectra and $K_d(490)$ in the region have been compared with those from VIIRS in 2012, 2016, and 2019, and shown consistent results (within ~5–10%). Using the GOCI daily statistical results from its hourly data, i.e., standard deviations (STDs) and coefficient of variations (CVs) of $nL_w(\lambda)$ and $K_d(490)$, the diurnal variability has been demonstrated and quantified. Over turbid coastal regions, STDs and CVs of $nL_w(\lambda)$ at GOCI 555 and 660 nm bands are important for characterizing diurnal variability, while for open oceans STDs and CVs of $nL_w(\lambda)$ at 412, 443, and 555 nm are useful. Specifically, using the four GOCI daily examples in 2019 on January 24, May 21, August 16, and November 15, we have carried out quantitative analyses for understanding regional diurnal variations. In addition, using the GOCI measurements from 2011 to 2020 in the region, hourly climatology $K_d(490)$ data in four seasons and quantitative results are derived and presented. Results show important characteristics in ocean diurnal variabilities over this highly dynamic and complex western Pacific Ocean region. Indeed, the regional diurnal variability has strong spatial and temporal (seasonal) dependences, which are mostly related to regional ocean optical and bio-optical properties.

1. Introduction

After the successful launch of NASA's Coastal Zone Color Scanner (CZCS) in the late 1970s (Gordon et al., 1980; Hovis et al., 1980), several global polar-orbiting ocean color satellites have been launched, including a series of the Visible Infrared Imaging Radiometer Suite (VIIRS) onboard the Suomi National Polar-orbiting Partnership (SNPP), NOAA-20, and NOAA-21 spacecrafts (Goldberg et al., 2013). One of the major advantages for polar-orbiting [or low Earth orbit (LEO)] satellites is their spatial coverage, i.e., global routine measurements. Such a capability is critical for providing global observations that are needed to understand and mitigate effects of global climate change. However, the observation frequency from polar-orbiting satellites is usually one to two times (or even less) per day over most global oceans and inland lakes. On the other hand, although limited in spatial coverage, satellite ocean property observations in the geostationary Earth orbit (GEO) have multiple measurements in its daily coverage (Fishman et al., 2012; IOCCG, 2012).

The Geostationary Ocean Color Imager (GOCI) began operation in 2010 onboard the Communication, Ocean, and Meteorological Satellite (COMS) flying at an altitude of 35,786 km, and has provided measurements at a local coverage of ~2,500×2,500 km^2 centered at 36°N and 130°E (Choi et al., 2012; Ryu et al., 2012). GOCI is the first GEO ocean color sensor and makes eight hourly measurements daily from local times between around 09:00–16:00. The GOCI total field of view (FOV) consists of 16 slots with 5,300×5,300 pixels in each image and a 500-m

* Corresponding author.
  E-mail address: Menghua.Wang@noaa.gov (M. Wang).

spatial resolution (Choi et al., 2012; Ryu et al., 2012).

Since 2010, GOCI has been providing ocean color observations in the western Pacific Ocean. Ocean property products have been produced with comparable data quality as those from the Moderate Resolution Imaging Spectroradiometer (MODIS) in highly turbid and complex regions (Concha et al., 2019; Park et al., 2022; Wang et al., 2013a). Indeed, GOCI enables an hourly monitoring of variations in coastal and inland waters in the region. Gap-free, high-temporal images of the diffuse attenuation coefficient at 490 nm [$K_d(490)$] can be achieved using the Data Interpolating Empirical Orthogonal Function (DINEOF) (Liu and Wang, 2016). The dynamics of sediment movements driven by the tide can be routinely mapped (Cheng et al., 2016). Diurnal dynamics and seasonal variations of suspended particulate matter (SPM) were characterized and quantified in coastal oceans and inland lakes (He et al., 2013; Huang et al., 2015; Liu et al., 2018). In a recent study, daily and diurnal net primary productivity (NPP) were also estimated from GOCI measurements (Wu et al., 2022). Using GOCI observations, diurnal ocean currents in the region were derived (Jiang and Wang, 2017; Yang et al., 2014). In addition, GOCI observations have been applied to identify and track algal blooms (Choi et al., 2014; Lou and Hu, 2014), monitor sea ice development (Yan et al., 2019), and detect regional marine fogs (Kim et al., 2020).

Due to its various applications and an increasing interest of multiple GEO observations per day, Korea launched a continuation of the GOCI mission, i.e., GOCI-II (Choi et al., 2018), in 2020. There are also geostationary ocean color missions planned, e.g., NOAA's Geostationary Extended Observations (GeoXO). The goal of this work is to further characterize and quantify some advantages of the geostationary satellites compared with those of LEO satellites, in terms of both the daily coverage and diurnal radiometric variability in coastal and open ocean regions. The GOCI observations from 2019 are employed to compare the daily composite of valid retrievals from eight shots between local times of 09:00–16:00 with those from VIIRS on the same day. Specifically, the diurnal variability of GOCI-derived normalize water-leaving radiance $nL_w(\lambda)$ and $K_d(490)$ in various regions during different seasons are studied to show the regional ocean diurnal variability. Furthermore, using the GOCI measurements from 2011 to 2020, hourly climatology $K_d(490)$ in four seasons are derived in the region, showing important diurnal variations. Therefore, daily multiple observations from geostationary satellites are the requisites to address and understand ocean diurnal variations and processes.

2. Data and methods

The GOCI measurements have been processed by the NOAA Ocean Color Science Team using the Multi-Sensor Level-1 to Level-2 (MSL12) satellite data processing system (Wang et al., 2013a), developed in the late 1990s to process ocean color data from multi-sensor measurements using the consistent algorithms and data processing package (Wang, 1999; Wang et al., 2002). GOCI has eight spectral bands from 412 to 865 nm, including the two near-infrared (NIR) bands. Considering that GOCI covers one of the most turbid world ocean regions (Shi and Wang, 2014) and does not contain the shortwave infrared (SWIR) bands for the effective atmospheric correction (Wang, 2007; Wang and Shi, 2007), an improved algorithm to iteratively adjust $nL_w(\lambda)$ at the two NIR bands (745 and 865 nm) was developed in MSL12 for GOCI data processing (Jiang and Wang, 2014; Wang et al., 2012). Therefore, we can properly account for the NIR reflectance contributions over turbid waters (Jiang and Wang, 2014; Wang et al., 2013a; Wang et al., 2012). In fact, GOCI data have been processed using the Jiang and Wang (2014) NIR algorithm in MSL12. Other data processing components, including the NIR atmospheric correction algorithm (Gordon and Wang, 1994; IOCCG, 2010), are the same for other satellite ocean color sensors, e.g., MODIS, VIIRS (Jiang and Wang, 2014; Wang et al., 2013a; Wang et al., 2013b). Results provide that GOCI-derived $nL_w(\lambda)$ and those from the in situ measurements are consistent (Wang et al., 2013a). Specifically, for this

highly turbid region, the mean $nL_w(\lambda)$ ratios at 412–680 nm between GOCI-derived and in situ-measured are reasonable and show similar data quality compared to those from MODIS (Wang et al., 2013a). It is also noted that, due to the lack (or unavailable) of the in situ data in the region, we have carried out the GOCI-VIIRS ocean color data comparisons across years in the period (2012, 2016, and 2019), showing consistent results across these years. Therefore, GOCI-measured ocean property products can be used effectively for monitoring the regional ocean variability and studying various diurnal ocean processes.

The same $K_d(490)$ algorithm (Wang et al., 2009) in VIIRS, MODIS, and other satellite sensors has been implemented and used for the GOCI ocean color data processing (Wang et al., 2013a). In fact, the $K_d(490)$ algorithm combines the empirical algorithm for open oceans (Mueller, 2000) and the semi-analytical $K_d(490)$ model for turbid coastal and inland waters (Wang et al., 2009). Specifically, the GOCI $K_d(490)$ algorithm uses GOCI-derived $nL_w(\lambda)$ at spectral bands of 490 and 555 nm for the open ocean empirical algorithm, and $nL_w(\lambda)$ at 490 and 660 nm for the turbid water model, with the two algorithms combined/blended (Wang et al., 2009) for deriving $K_d(490)$ over the GOCI-measurement domain.

In this work, we use GOCI and VIIRS observations for the entire 2019 year in this region to analyze and evaluate the valid ocean color retrievals extracted from GOCI, compared to those from VIIRS. The $nL_w(\lambda)$ spectra and $K_d(490)$ diurnal variabilities for various regions are assessed and quantified. As noted previously, the same $K_d(490)$ algorithm (Wang et al., 2009) has been used for both GOCI and VIIRS. The analysis provides detailed characterization and quantification of some important benefits of geostationary satellites, compared to polar-orbiting observations. The diurnal variations of GOCI-derived $nL_w(\lambda)$ and $K_d(490)$ from 09:00–16:00 are characterized with standard deviation (STD) and the coefficient of variation (CV) for $nL_w(\lambda)$ (i.e., STD[$nL_w(\lambda)$] and CV [$nL_w(\lambda)$]) at 443, 555, and 660 nm, as well as $K_d(490)$ (i.e., STD [$K_d(490)$] and CV[$K_d(490)$]). Using the GOCI observations in January, April, July, and October from 2011 to 2020, we compute the hourly climatology GOCI $K_d(490)$ retrievals in eight shots from 09:00–16:00. We also chose GOCI observations on January 24, May 21, August 16, and November 15 in 2019 as examples to study the diurnal variability with seasonal dependence.

3. Results

3.1. Coverage of GOCI and VIIRS retrievals

As an example, using the GOCI-derived $nL_w(555)$ on March 17, 2019, Fig. 1 shows the retrieval coverage for the entire GOCI domain at local times of 09:00–16:00 as shown in Fig. 1a–1h, respectively. Most of the unavailable GOCI retrievals in Fig. 1 were caused by cloud coverage. The change of cloud coverage in the GOCI measurement domain from 09:00–16:00 was remarkable. At local times between 09:00 and 12:00, most parts of the Bohai Sea (BS), Yellow Sea (YS), East China Sea (ECS), and Sea of Japan (East Sea) were cloud free (Fig. 1a–1d). In contrast, most of these regions were cloud covered around 16:00, thereby showing no ocean color retrievals (Fig. 1h). It is noted that other unfavorable conditions also cause the missing ocean color retrievals (Mikelsons and Wang, 2019), e.g., high sun glint contaminations, large solar-zenith angles (>70°) (Mikelsons et al., 2020), straylight and cloud shadow contaminations (Jiang and Wang, 2013), etc.

The cloud coverage changes in the GOCI eight shots between 09:00 and 16:00 make GOCI observations to have more valid daily retrievals in comparison to a polar-orbiting satellite. Fig. 2a is the daily composite of $nL_w(555)$ from eight GOCI observations on March 17, 2019. In comparison to GOCI $nL_w(555)$ retrievals from the individual shot (e.g., Fig. 1e), the valid $nL_w(555)$ pixels were significantly increased from the GOCI daily composite $nL_w(555)$ image (Fig. 2a). Fig. 2b shows the $nL_w(551)$ image acquired from VIIRS on the same day. Unlike GOCI daily composite $nL_w(555)$ in Fig. 2a, there were no VIIRS daily $nL_w(551)$
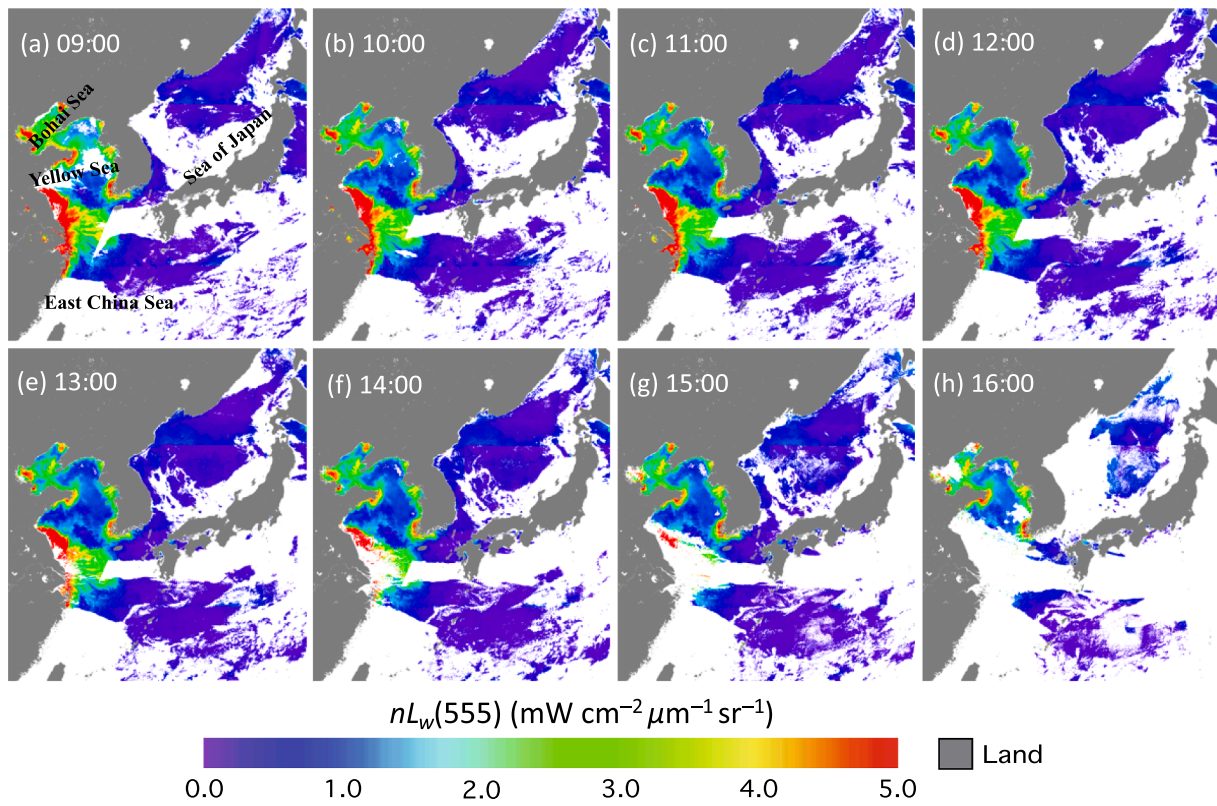
Fig. 1. GOCI-derived nL_w(555) in the entire GOCI domain from different shots on March 17, 2019, at around local time noted (a)–(h) for 09:00–16:00.
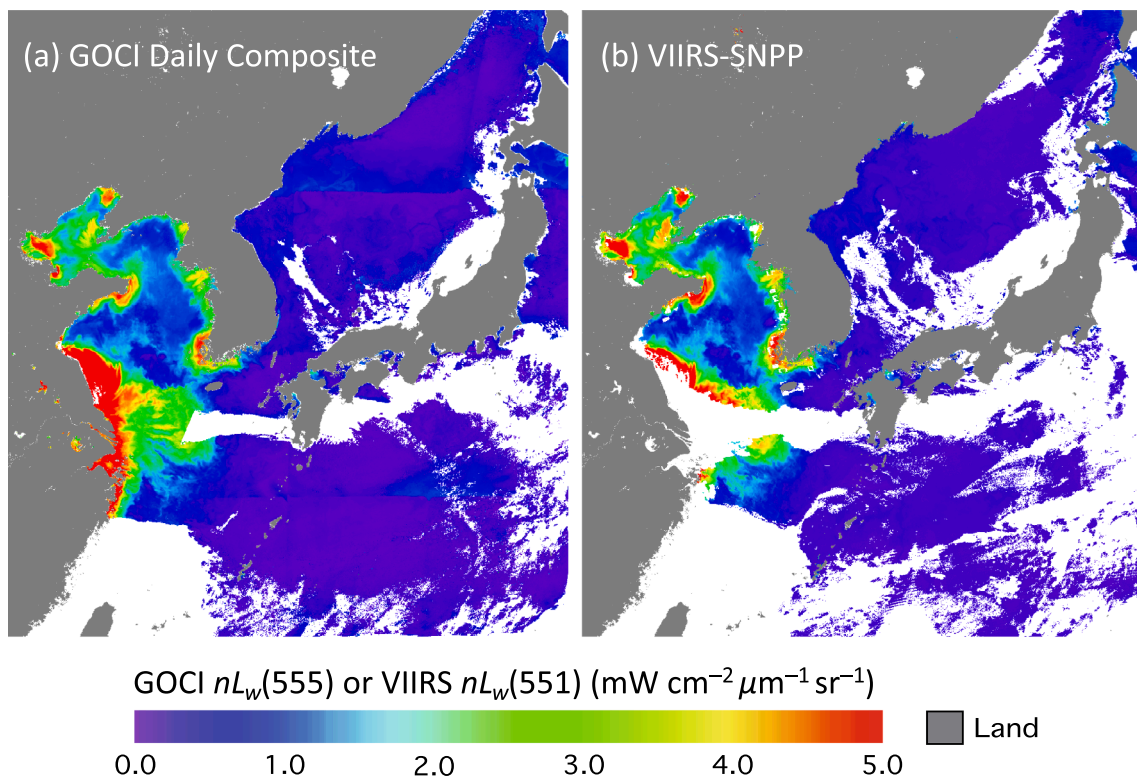

Fig. 2. (a) GOCI-derived daily composite of nL_w(555) from eight shots between 09:00 and 16:00 on March 19, 2019, and (b) VIIRS-SNPP-derived nL_w(551) on the same day.

retrievals in coastal oceans of the YS and ECS (Fig. 2b). In addition, there were much fewer valid $nL_w(551)$ in the open ocean from VIIRS in Fig. 2b, compared to those from GOCI-derived $nL_w(555)$ daily composite (Fig. 2a).

Fig. 3 provides a quantitative evaluation of the coverage for valid GOCI retrievals in the entire domain for each GOCI shot from 09:00–16:00 in 2019. Note that, at 15:00 (Fig. 3g) and 16:00 (Fig. 3h),

there were sparse or even no GOCI ocean color data between late autumn and early spring due to cases associated with large solar-zenith angles (Mikelsons et al., 2020). This is particularly true for GOCI measurements around 16:00. Ocean color retrievals are masked out for cases with solar-zenith angle > 70° due to associated large errors (Mikelsons et al., 2020). For all GOCI shots from 09:00–15:00, the valid GOCI ocean color retrievals are generally similar at ~20%, while there are
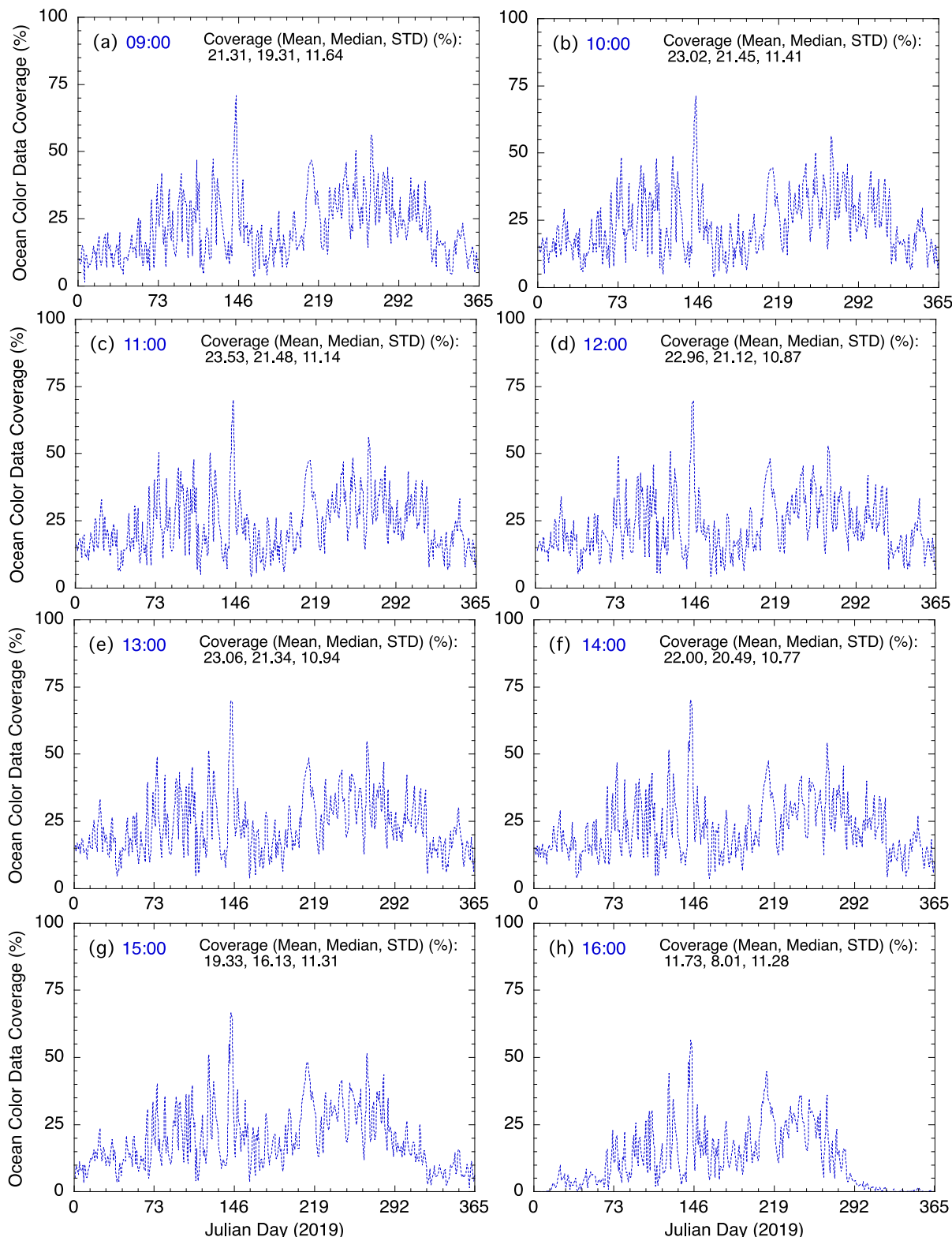

Fig. 3. Coverage (%) of GOCI-derived ocean color retrievals in daily (Julian day) time series of 2019 for the shot of local time noted (a)–(h) for 09:00–16:00.

significantly lower retrievals of ~10% around 16:00. The seasonal variation of valid GOCI retrievals is with a low data coverage in the summer season, while it is high in spring and autumn seasons. This reflects the fact that the GOCI covered region usually has more cloud coverage in summer, compared to that in spring and autumn seasons.

Table 1 provides statistical results of mean, median, and STD for ocean color data coverage (%) for each shot from 09:00–16:00 in 2019. In computing statistical results, data from the entire 2019 year in the region were used (i.e., Fig. 3). Results in Table 1 show that the number of retrievals in the region is generally quite stable from 09:00–14:00, around 21–23%. However, there is a noticeable drop at 15:00 (~19%), and particularly at 16:00 the number of retrievals (~12%) deceased significantly due to cases associated with large solar-zenith angles in late autumn, winter, and early spring (Fig. 3h).

It is also interesting to note that, based on results in Table 1, the optimal coverage of ocean color retrievals in the region is around 10:00–11:00 and 12:00–13:00, corresponding to the preferred morning and afternoon orbitals for satellite remote sensing.

Fig. 4a provides a time series of the daily data coverage (%) in 2019 from the GOCI measurements compared to those from VIIRS. The GOCI daily data coverage was about doubled in relation to a GOCI single shot. Indeed, GOCI daily composite data can provide significantly more valid ocean color retrievals in comparison to those from a polar-orbiting satellite. In 2019, the coverage of the valid GOCI daily composite data normally ranged between ~20% and ~80% (Fig. 4a). For VIIRS, however, the data coverage ranged between ~10% and ~50% (Fig. 4a).

We note that for VIIRS, the data coverage in the summer season was generally below ~20%, which was significantly less than that in other seasons due to more clouds and substantially more cases with high sun glint contaminations (Mikelsons et al., 2020). This is demonstrated in Fig. 4b, which compares coverage of ocean color retrievals between GOCI at the 13:00 shot and VIIRS in the 2019 summer days. It is noted that GOCI measurements around 13:00 are the closest GOCI observations with VIIRS overpasses in the region. Results in Fig. 4b show that GOCI measurements at 13:00 usually have more retrievals than those from VIIRS, mainly because of the sun glint contamination issue for VIIRS. Indeed, results in Table 2 show that the mean GOCI daily coverage values are 44.90%, 44.89%, 51.96%, and 33.39% in spring, summer, fall, and winter, respectively, while the corresponding VIIRS values are 23.56%, 17.15%, 28.01%, and 18.55%, respectively. These seasonable coverage values can be compared with those of the GOCI single shot at 13:00 as 25.87%, 22.75%, 27.26%, and 16.50%, respectively. Table 2 also provides statistical results of the GOCI single shot at 10:00 (morning), which are comparable to those at 13:00 (afternoon). As shown in Table 2, the mean coverage of valid GOCI retrievals in the daily composite in 2019 was ~43.81% (with ~21.31% and ~23.06% for the single shot at 10:00 and 13:00, respectively), while it was ~21.77% from VIIRS.

3.2. Regional ocean diurnal variability

3.2.1. GOCI- and VIIRS-measured $nL_w(\lambda)$ and $K_d(490)$

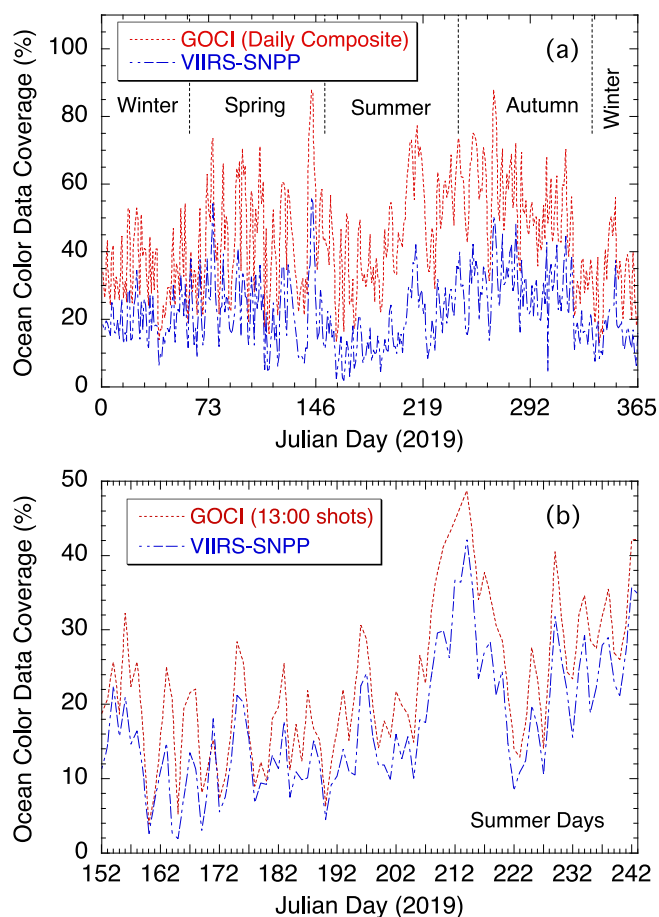At NOAA, both GOCI and VIIRS data have been routinely processed

Fig. 4. Comparisons of the daily coverage (%) of ocean color retrievals in the GOCI domain as a function of Julian day between measurements from GOCI and VIIRS for (a) GOCI daily composite over entire 2019 and (b) GOCI shot at 13:00 for the 2019 summer days.

using the same MSL12 ocean color data processing software (Wang et al., 2013a; Wang et al., 2013b). The GOCI products from MSL12 are generally consistent with the in situ measurements (Wang et al., 2013a; Wang et al., 2012), and VIIRS ocean color products have also been well calibrated (Sun and Wang, 2015; Wang et al., 2016) and validated (Barnes et al., 2019; Mikelsons et al., 2020; Wang et al., 2020). To further validate the 2019 GOCI data products used in this study, quantitative comparisons and evaluations were also conducted between VIIRS and the corresponding GOCI measurements. Results show that over the GOCI coverage area the ocean color data from GOCI and VIIRS are consistent.

Fig. 5 provides an example of GOCI and VIIRS ocean color products on May 21, 2019. Results in Fig. 5 show that, in their spatial pattern and magnitude, GOCI-derived $nL_w(412)$, $nL_w(443)$, $nL_w(490)$, $nL_w(555)$, $nL_w(660)$, and $K_d(490)$ (Fig. 5a–5f) at the time around 13:00 agree well with the corresponding VIIRS-measured $nL_w(410)$, $nL_w(443)$, $nL_w(486)$, $nL_w(551)$, $nL_w(671)$, and $K_d(490)$ (Fig. 5g–5l), respectively. To have quantitative evaluations and characterizations of ocean properties, as well as GOCI and VIIRS ocean color data comparisons, four pseudo-stations as noted in Fig. 5a are defined, i.e., station A in the Subei Shoal region, station B in the offshore sediment plume in the ECS, station C in open oceans of the ECS, and station D in the BS region. The selection of these four stations can properly represent both coastal and offshore waters as well as open oceans in the BS, YS, and ECS regions.

The MSL12-derived GOCI products were validated with the in situ measurements in the early 2010s (Wang et al., 2013a). To further quantify data accuracy and evaluate the capability of using GOCI data to

Table 1
Statistical results (mean, median, and STD) of ocean color data coverage in the GOCI domain for eight different shots in 2019.

Shot Time	Mean (%)	Median (%)	STD (%)
09:00	21.31	19.31	11.64
10:00	23.02	21.45	11.41
11:00	23.53	21.48	11.14
12:00	22.96	21.12	10.87
13:00	23.06	21.34	10.94
14:00	22.00	20.49	10.77
15:00	19.33	16.13	11.31
16:00	11.73	8.01	11.28

Table 2
Statistical results (mean and STD) of valid retrievals for four seasons in 2019 and entire 2019 year from daily GOCI composite, GOCI 10:00 shot, GOCI 13:00 shot, and daily VIIRS.

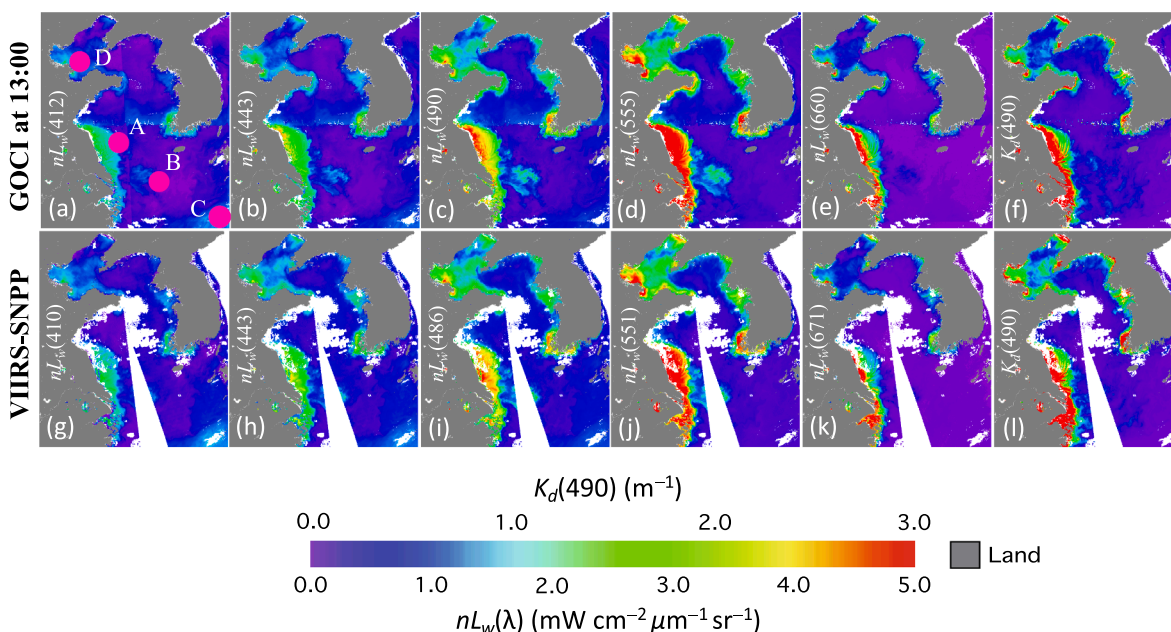| Season	GOCI Mean & STD (%)						VIIRS (%)	
	Daily		10:00 Shot		13:00 Shot		Daily	
	Mean	STD	Mean	STD	Mean	STD	Mean	STD
Spring	44.90	25.75	25.75	13.79	25.87	13.67	23.56	11.50
Summer	44.89	21.77	21.77	10.13	22.75	9.84	17.15	8.84
Autumn	51.96	28.83	28.83	10.20	27.26	9.83	28.01	9.51
Winter	33.39	15.86	15.86	5.91	16.50	5.91	18.55	6.36
All Year	43.81	21.31	21.31	11.64	23.06	10.94	21.77	10.15

Fig. 5. Comparison of the satellite ocean color retrievals on May 21, 2019, between GOCI at 13:00 and VIIRS for (a, g) $nL_w(412)$ and $nL_w(410)$, (b, h) $nL_w(443)$, (c, i) $nL_w(490)$ and $nL_w(486)$, (d, j) $nL_w(555)$ and $nL_w(551)$, (e, k) $nL_w(660)$ and $nL_w(671)$, and (f, l) $K_d(490)$. Note that the pseudo stations A (33.55°N, 121.79°E) in the Subei Shoal of the YS, B (31.90°N, 124.72°E) in the ECS offshore plume, C (29.42°N, 128.25°E) in the open ocean of the ECS, and D (38.44°N, 119.23°E) in the BS are marked in panel a.

characterize the regional diurnal variability, we compare GOCI-derived (at 13:00) and VIIRS-measured $nL_w(\lambda)$ spectra and $K_d(490)$ in 2012, 2016, and 2019 (across from early to recent years). Fig. 6a–6c provides scatter plot comparisons of GOCI- and VIIRS-derived $nL_w(\lambda)$ spectra, from 2012 (Fig. 6a), 2016 (Fig. 6b), and 2019 (Fig. 6c), at stations of A, B, C, and D (noted in Fig. 5a). Results show that GOCI- and VIIRS-derived $nL_w(\lambda)$ spectra are generally consistent and comparable. Some quantitative statistical comparisons (ratios in mean, median, and STD) are also noted in Fig. 6a–6c, as well as in Table 3, showing that in 2019 the mean ratios of $nL_w(\lambda)$ between GOCI and VIIRS are 0.940, 0.925, 0.964, 1.032, and 1.016 for GOCI spectral bands at 412, 443, 490, 555, and 660 nm, respectively, with an overall $nL_w(\lambda)$ ratio of 0.975 for all five bands (Fig. 6c and Table 3). The corresponding mean $nL_w(\lambda)$ ratios for the year 2012 are 1.070, 1.083, 1.037, 1.046, and 1.030, with an overall $nL_w(\lambda)$ ratio of 1.053 (Fig. 6a and Table 3). For the year 2016, these mean $nL_w(\lambda)$ ratios are 0.983, 0.989, 0.971, 1.016, and 1.019, with an overall $nL_w(\lambda)$ ratio of 0.995 (Fig. 6b and Table 3). It is noted that results in 2012 can be related to the early GOCI validation results using the in situ measurements (Wang et al., 2013a). Therefore, although there are some differences, MSL12-derived GOCI $nL_w(\lambda)$ spectra are generally reasonable and consistent with those from VIIRS across years 2012–2019, with their mean differences for all $nL_w(\lambda)$ usually within ~5–10%.

Similarly, we have quantitatively compared MSL12-derived GOCI

$K_d(490)$ (at 13:00) with those from VIIRS-SNPP in 2012, 2016, and 2019 (across different years of the GOCI mission). Fig. 6d shows scatter plot comparisons of the GOCI-derived $K_d(490)$ (at 13:00) with those from VIIRS-SNPP at stations A, B, C, and D in 2012, 2016, and 2019. Statistical results in Fig. 6d and Table 3 show that mean ratios between GOCI- and VIIRS-derived $K_d(490)$ for 2012, 2016, and 2019 are 1.05, 1.037, and 0.964, respectively, with STD values of 0.195, 0.200, and 0.275, respectively. Therefore, Fig. 6d and Table 3 show that GOCI-derived $K_d(490)$ are generally consistent with those from VIIRS and their mean differences are usually within ~5%.

It should be noted that there are some slight differences at the band nominal center wavelengths between GOCI (412, 443, 490, 555, and 660 nm) and VIIRS-SNPP (410, 443, 486, 551, and 671 nm). We have calculated the sensor spectral response function (SRF) weighted Rayleigh (air molecules) optical thickness (Wang, 1999) for GOCI and VIIRS-SNPP at the corresponding five spectral bands, and computed ratios of SRF-weighted Rayleigh optical thickness between GOCI and VIIRS-SNPP. The five corresponding ratios are 1.003, 1.008, 0.974, 0.958, and 1.052 for the GOCI (VIIRS) spectral bands of 412 (410), 443 (443), 490 (486), 555 (551), and 660 (671) nm, respectively. Therefore, some differences may be at the green and red bands.

It is also noted that, in addition to several extensive validation efforts (Barnes et al., 2019; Mikelsons et al., 2020; Wang et al., 2020), VIIRS ocean color products are being routinely monitored and evaluated using various
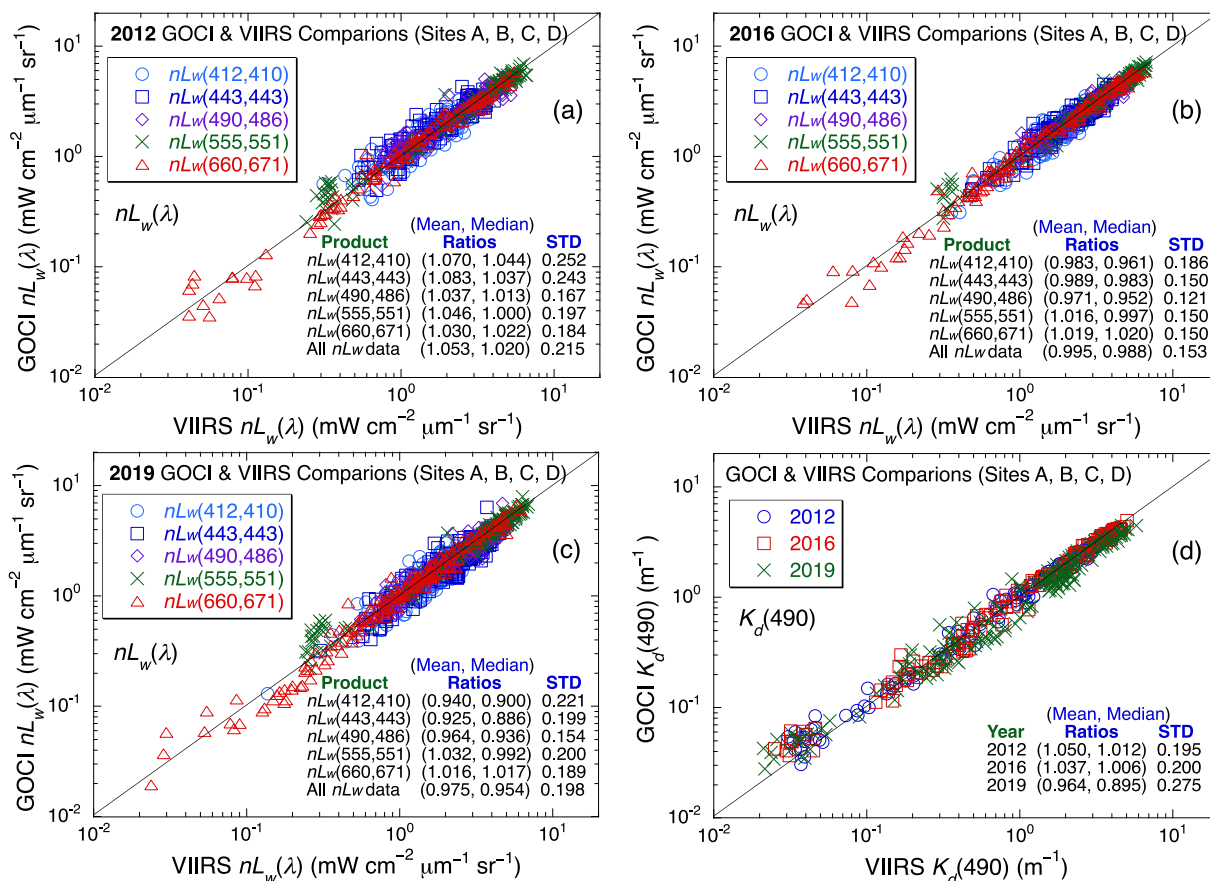
Fig. 6. Scatter plot of GOCI-derived $nL_w(\lambda)$ (at 13:00) compared with those from VIIRS-SNPP at stations A, B, C, and D (marked in Fig. 5a) for years of (a) 2012, (b) 2016, and (c) 2019. Plot d shows GOCI-derived $K_d(490)$ (at 13:00) compared with those from VIIRS-SNPP at stations A, B, C, and D for years of 2012, 2016, and 2019. Statistical results in mean and median ratios (unitless), as well as ratio STD (unitless), between GOCI- and VIIRS-derived $nL_w(\lambda)$ (at the five spectral bands) and $K_d(490)$ are provided in the plots (also shown in Table 3).

Table 3
Statistical results from scatter plots in Fig. 6 (mean, median, STD, and number of matchups N) of GOCI-derived (at 13:00) versus VIIRS-derived $nL_w(\lambda)$ and $K_d(490)$ at stations A, B, C, and D (noted in Fig. 5a) for years 2012, 2016, and 2019.

Parameter	Statistical Results in $nL_w(\lambda)$ & $K_d(490)$ Ratio (GOCI vs. VIIRS)											
	2012				2016				2019			
	Mean	Median	STD	N	Mean	Median	STD	N	Mean	Median	STD	N
$nL_w(412,410)$	1.070	1.044	0.252	121	0.983	0.961	0.186	138	0.940	0.900	0.221	173
$nL_w(443,443)$	1.083	1.037	0.243	126	0.989	0.983	0.150	138	0.925	0.886	0.199	190
$nL_w(490,486)$	1.037	1.013	0.167	131	0.971	0.952	0.121	141	0.964	0.936	0.154	195
$nL_w(555,551)$	1.046	1.000	0.197	127	1.016	0.997	0.150	140	1.032	0.992	0.200	192
$nL_w(660,671)$	1.030	1.022	0.184	114	1.019	1.020	0.150	131	1.016	1.017	0.189	175
All $nL_w(\lambda)$	1.053	1.020	0.215	619	0.995	0.988	0.153	688	0.975	0.954	0.198	925
$K_d(490)$	1.050	1.012	0.195	122	1.037	1.006	0.200	140	0.964	0.895	0.275	178

in situ data (https://www.star.nesdis.noaa.gov/socd/mecb/color/). Therefore, VIIRS ocean color data can be well used as references to evaluate GOCI ocean color products. Furthermore, we examined the monthly composite of GOCI $nL_w(\lambda)$ and $K_d(490)$ products from 2011 to 2020, and there are no obvious long-term trends of these products (as also shown in Fig. 6 and Table 3). This provides further evidence that the GOCI sensor degradation over the 10-year period has been reasonably characterized, and the validation and assessment of the GOCI products in the early period of the GOCI mission (Wang et al., 2013a) still reasonably holds in 2019 (Fig. 6 and Table 3).

3.2.2. An example of the diurnal variability

Using eight GOCI measurements from 09:00–16:00 on May 21, 2019, Fig. 7 shows the diurnal variation of GOCI-derived $nL_w(443)$

(Fig. 7a–7h), $nL_w(555)$ (Fig. 7i–7p), $nL_w(660)$ (Fig. 7q–7x), and $K_d(490)$ (Fig. 7y–7ff). The diurnal variations in $nL_w(\lambda)$ spectra reflected the regional optical, biological, and biogeochemical processes and changes. The daily eight observations of ocean color properties were similar in both spatial pattern and magnitudes. However, differences among various GOCI shots were discernable. In highly turbid regions of the ECS and YS, extremely high $nL_w(660) > \sim5$ mW cm^{-2} μm^{-1} sr^{-1} (Fig. 7q–7x) and $K_d(490) > 3$ m^{-1} (Fig. 7y–7ff) gradually decreased from 09:00 (Fig. 7q and 7y) to 15:00 (Fig. 7w and 7ee), and then increased around 16:00 (Fig. 7x and 7ff). However, in the open ocean region, where $nL_w(660)$ values were usually small, differences among GOCI inter-shot measurements in ocean properties were trivial and unnoticeable.

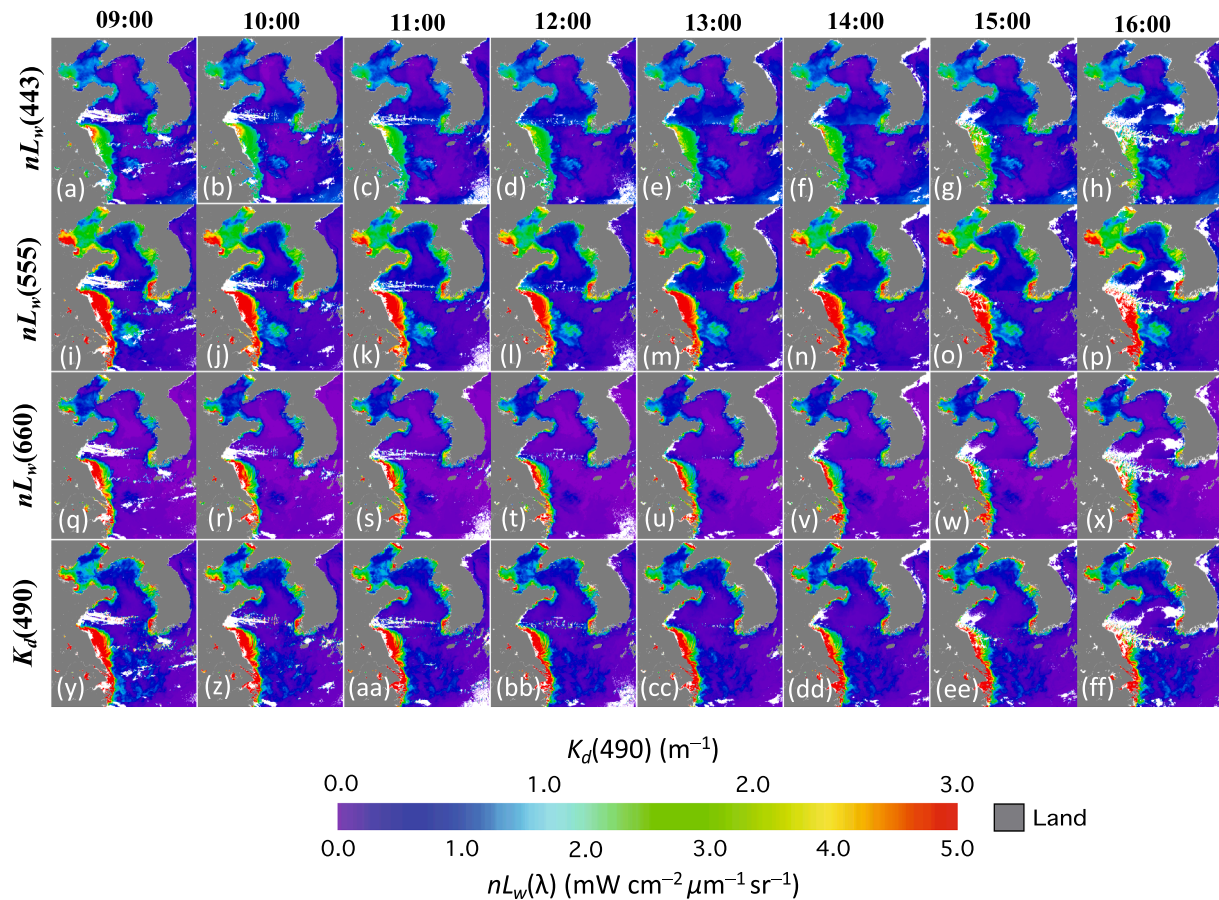In comparison to qualitative evaluations in Fig. 7, diurnal variations

Fig. 7. GOCI ocean color retrievals at local times from 09:00–16:00 on May 21, 2019, in the BS, YS, and ECS for (a–h) $nL_w(443)$, (i–p) $nL_w(555)$, (q–x) $nL_w(660)$, and (y–ff) $K_d(490)$.

of these water properties are clearly shown for different ocean regions in Fig. 8. At station A (Fig. 8a and 8b), $nL_w(\lambda)$ generally dropped from 09:00 to around 13:00–15:00. More significant diurnal variabilities could be found for $nL_w(\lambda)$ at 555, 660, and 680 nm. Indeed, $nL_w(660)$ showed the most significant changes from ~2.5–3.0 mW cm^{-2} μm^{-1} sr^{-1} at 09:00 to ~1.0–1.5 mW cm^{-2} μm^{-1} sr^{-1} at 15:00. Between 15:00 and 16:00, $nL_w(660)$ jumped to ~3.0 mW cm^{-2} μm^{-1} sr^{-1}. Similarly, $K_d(490)$ decreased from ~2.5 m^{-1} at 09:00 to < ~1.0 m^{-1} at 15:00, and then it increased to > ~3.0 m^{-1} at 16:00. As expected, diurnal variations of $nL_w(\lambda)$ and $K_d(490)$ were in phase with the change of the highly turbid water coverage as shown in Fig. 7.

The sediment plume in the central ECS is an important feature due to strong vertical mixing, sediment re-suspension, and shallow water bathymetry (Bi et al., 2011; Dong et al., 2011; Doxaran et al., 2014). Fig. 8c and 8d shows the diurnal variation in $nL_w(\lambda)$ at station B on May 21, 2019. It is noted that scales in $nL_w(\lambda)$ for Fig. 8a and 8b, 8c and 8d, 8e and 8f, and 8g and 8h are different, representing the regional differences in ocean optical properties (Shi and Wang, 2014). In comparison to station A, $nL_w(\lambda)$ were relatively stable from 09:00–16:00. We note that the diurnal variation of $nL_w(\lambda)$ at station B was not same as that at station A (Fig. 8a and 8b), due to different water property (Shi and Wang, 2014). At station C, the open ocean region (Fig. 8e and 8f), $nL_w(\lambda)$ show a typical optical feature for clear oceans with some diurnal variations. $K_d(490)$ in the site were low at ~0.05 m^{-1} between 09:00 and 16:00 with little diurnal changes. In the BS at station D (Fig. 8g and 8h), diurnal variations of $nL_w(\lambda)$ at 555, 660, and 680 nm were a little more notable than those at the short-blue/blue bands of $nL_w(412)$ and $nL_w(443)$ (Fig. 8h), while $K_d(490)$ at station D decreased from ~1.3 m^{-1} at 09:00 to < ~0.6 m^{-1} at 16:00. The GOCI-derived $nL_w(\lambda)$ and $K_d(490)$ at these four stations show that diurnal variations of ocean properties

are both time-sensitive and regional-dependent. This implies that ocean properties are driven by a variety of atmosphere and ocean forcings, as well as their processes, such as winds, tides, currents, etc., and therefore, the capability of daily satellite multiple observations is a requisite to catch and monitor the diurnal variations for this highly dynamic coastal and near-shore ocean region.

3.2.3. Statistical analysis

The diurnal variations of GOCI-derived $nL_w(\lambda)$ and $K_d(490)$ from 09:00–16:00 are further characterized with STD[$nL_w(443)$], STD[$nL_w(555)$], STD[$nL_w(660)$], and STD[$K_d(490)$] in Fig. 9a–9d, respectively. In turbid regions of the YS and ECS, $nL_w(\lambda)$ and $K_d(490)$ experienced significant diurnal variability. Specifically, STD[$nL_w(660)$] reached > ~1 mW cm^{-2} μm^{-1} sr^{-1} and STD[$K_d(490)$] was also ~1 m^{-1} along the Subei Shore region. In the offshore region, STD[$nL_w(\lambda)$] and STD[$K_d(490)$] were generally small (as expected), which were well represented in Fig. 9a–9d. It is also noted that the sediment plume off the ECS, the wiggling pattern of STD[$nL_w(\lambda)$] and STD[$K_d(490)$] in Fig. 9a–9d, reflected the dynamics in the offshore sediment plume and the movement of sediment front from 09:00–16:00 on May 21, 2019. Some quantitative values (mean and median) of STD[$nL_w(\lambda)$] and STD[$K_d(490)$] over the entire coverage region from Fig. 9a–9d are provided in Table 4.

Furthermore, Fig. 9e–9h shows the coefficient of variation (CV) for $nL_w(\lambda)$ (i.e., CV[$nL_w(\lambda)$]) at 443, 555, and 660 nm, and $K_d(490)$ on May 21, 2019, i.e., CV[$nL_w(443)$] (Fig. 9e), CV[$nL_w(555)$] (Fig. 9f), CV[$nL_w(660)$] (Fig. 9g), and CV[$K_d(490)$] (Fig. 9h), respectively. CV values represent mostly relative changes in diurnal variations in these parameters. In a large part of the turbid coastal regions in the ECS, YS, and BS, CVs were below ~0.3 due to the enhanced mean values of $nL_w(\lambda)$ and
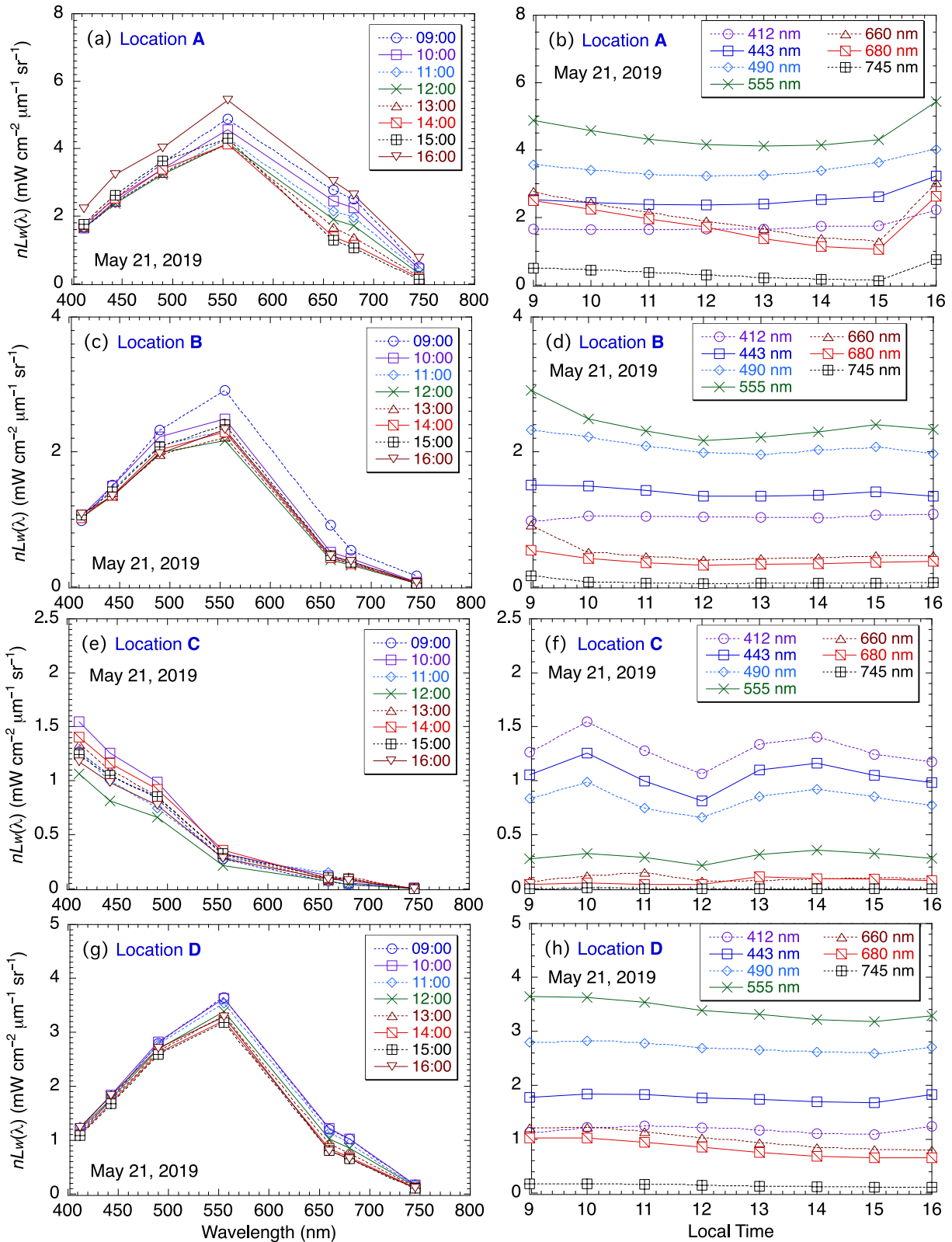
Fig. 8. Quantitative evaluations of the diurnal variation of GOCI-derived $nL_w(\lambda)$ spectra (a, c, e, and g) and the hourly variation of GOCI-derived $nL_w(\lambda)$ at the GOCI bands (b, d, f, and h) on May 21, 2019, from 09:00–16:00 at the location of (a and b) station A, (c and d) station B, (e and f) station C, and (g and h) station D.

$K_d(490)$. In the offshore regions, however, CVs were generally similar to those in the coastal regions for $CV[nL_w(555)]$ (Fig. 9f) in the range of ~0.1–0.2. Values of $CV[nL_w(443)]$ (Fig. 9e) and $CV[nL_w(660)]$ (Fig. 9g) were ~0.6 in open oceans and offshore regions, while they were ~0.1–0.2 in the coastal regions. Corresponding to Fig. 9e–9h, Table 4

provides mean and median values of $CV[nL_w(\lambda)]$ and $CV[K_d(490)]$ for GOCI measurements on May 21, 2019, over the entire coverage (Fig. 9e–9h).
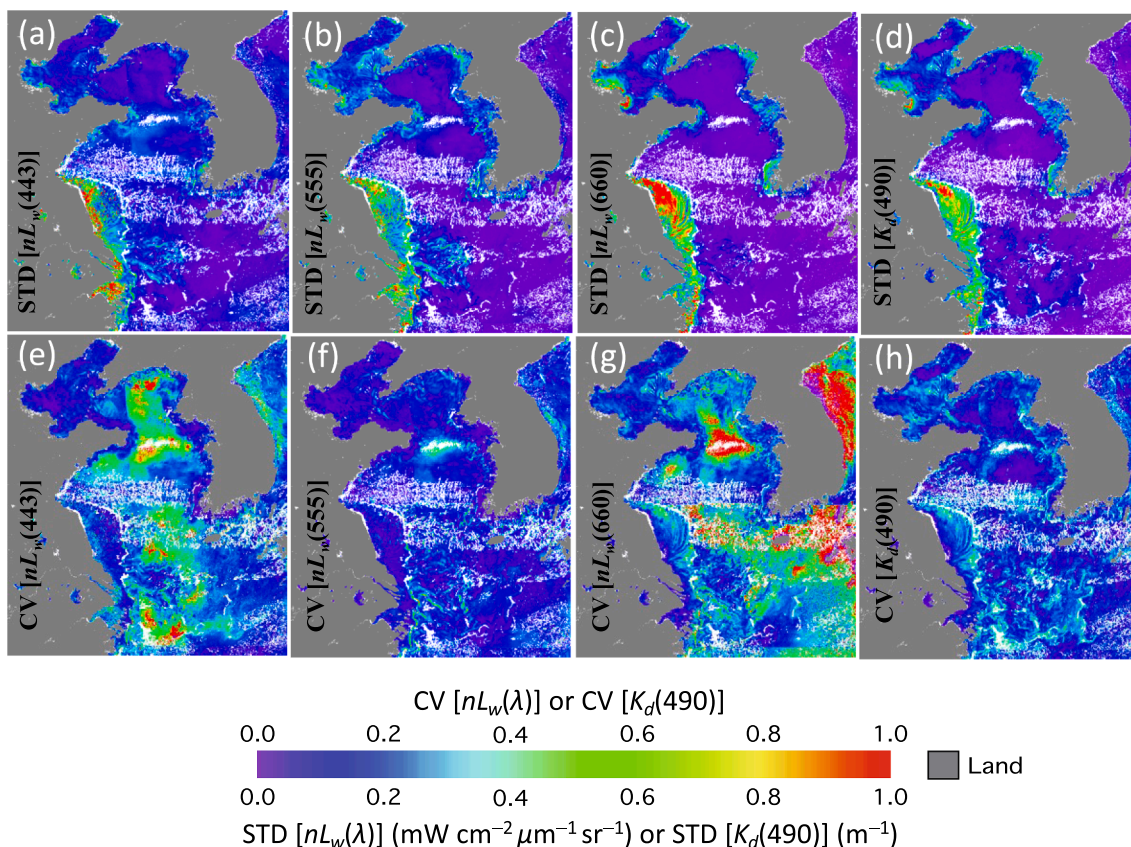
Fig. 9. Pixelwise daily STD and CV from GOCI eight shots on May 21, 2019, in the BS, YS, and ECS for (a, e) $nL_w(443)$, (b, f) $nL_w(555)$, (c, g) $nL_w(660)$, and (d, h) $K_d(490)$.

Table 4
Statistical results of daily STD and CV of GOCI-derived $nL_w(\lambda)$ and $K_d(490)$ from GOCI eight shots on May 21, 2019.

Parameter	STD-Mean*	STD-Median*	CV-Mean	CV-Median
$nL_w(412)$	0.135	0.097	0.483	0.329
$nL_w(443)$	0.136	0.092	0.269	0.209
$nL_w(490)$	0.127	0.076	0.143	0.116
$nL_w(555)$	0.128	0.059	0.125	0.103
$nL_w(660)$	0.087	0.019	0.421	0.261
$K_d(490)$	0.129	0.055	0.182	0.142

*Unit: mW cm^{-2} μm^{-1} sr^{-1} for $nL_w(\lambda)$ and m^{-1} for $K_d(490)$.

3.2.4. Discussion about STDs and CVs

The diurnal variabilities of $nL_w(\lambda)$ and $K_d(490)$ represented with STD [$nL_w(\lambda)$ or $K_d(490)$] and CV[$nL_w(\lambda)$ or $K_d(490)$] contain both the real diurnal variability of $nL_w(\lambda)$ and $K_d(490)$ signals and their uncertainties caused by the GOCI sensor calibration and MSL12 data processing system. In fact, STD values show regional diurnal variations in their magnitude changes, while CVs provide diurnal variability in a relative sense. Therefore, for highly turbid coastal oceans, both STDs and CVs of $nL_w(555)$, $nL_w(660)$, and $K_d(490)$ (i.e., water optical information at green/red bands and even at the NIR bands) are important for measurements of diurnal variations. For open oceans, on the other hand, STDs and CVs of $nL_w(443)$ and $nL_w(555)$ (i.e., ocean optical information at short-blue/blue and green bands) are useful.

To further get the sense of the regional diurnal variation with the statistical analysis, it is important to quantify STDs and CVs at several specific locations representing different water properties. Table 5 provides mean STDs and CVs for stations A, B, C, and D, which are noted in Fig. 5a. In computing these values, we have used 5×5 pixels at the locations and values of STD[$nL_w(\lambda)$ or $K_d(490)$] and CV[$nL_w(\lambda)$ or $K_d(490)$] are then calculated (Table 5). Results in Table 5 show that there are high diurnal variations at location A (highly turbid waters) with the highest STD[$nL_w(660)$] and STD[$K_d(490)$] from the four sites. On the other hand, at the open ocean location C, STD[$nL_w(660)$] and STD[$K_d(490)$] are the smallest among the four sites with noticeable STDs and CVs at the short-blue/blue bands, as well as high CVs at the green band. STDs and CVs for locations B and D have mixed values, i.e., there are moderately

Table 5
Statistical results of daily STD and CV of GOCI-derived $nL_w(\lambda)$ and $K_d(490)$ from GOCI eight shots at stations A, B, C, and D (noted in Fig. 5a) on May 21, 2019.

Parameter	STD* at Station				CV at Station			
	A	B	C	D	A	B	C	D
$nL_w(412)$	0.241	0.156	0.165	0.068	0.130	0.147	0.127	0.057
$nL_w(443)$	0.290	0.226	0.132	0.070	0.105	0.158	0.121	0.040
$nL_w(490)$	0.285	0.310	0.104	0.094	0.074	0.147	0.122	0.034
$nL_w(555)$	0.294	0.301	0.049	0.187	0.058	0.128	0.157	0.055
$nL_w(660)$	0.502	0.100	0.022	0.178	0.211	0.221	0.253	0.174
$K_d(490)$	0.426	0.059	0.013	0.271	0.205	0.210	0.264	0.259

*Unit: mW cm^{-2} μm^{-1} sr^{-1} for $nL_w(\lambda)$ and m^{-1} for $K_d(490)$.

high diurnal ocean variations in the regions. Therefore, these STDs and CVs provide quantitative measures for the regional diurnal variations.

3.3. Diurnal variability with seasonal dependence

3.3.1. A winter day example

As an example presented in Figs. 7–9 and Tables 4 and 5 for the diurnal variabilities of $nL_w(\lambda)$ and $K_d(490)$ on a spring day on May 21, 2019, Figs. 10–12 further show the diurnal variabilities in other seasonal days on January 24, 2019 (winter), August 16, 2019 (summer), and November 15, 2019 (autumn), respectively. Note that there were limited satellite ocean color retrievals in the early morning (09:00) (a winter day in Fig. 10) and late afternoon (16:00) (winter and autumn days in Figs. 10 and 12), due to cases related to large solar-zenith angles.

On January 24, 2019, the spatial patterns of $nL_w(\lambda)$ and $K_d(490)$ from 09:00–16:00 were generally similar in coastal regions (Fig. 10). Note that some significant missing data at 09:00, 15:00, and 16:00 were due to cases associated with large solar-zenith angles (Mikelsons et al., 2020). Such cases can be identified from image comparisons with those from the nearby time shots, e.g., Fig. 10a to Fig. 10b and 10c or Fig. 10h to Fig. 10g and 10f. In the BS, gradually increasing cloud coverage was observed from 10:00 to 14:00. For a large portion of the YS, $nL_w(555)$ dropped noticeably from 10:00 to 14:00 (Fig. 10j–10n). For the $nL_w(660)$ distribution in Fig. 10q–10x, an area with $nL_w(660) > \sim3$ mW cm^{-2} μm^{-1} sr^{-1} along the coastal region of the ECS shrank from 09:00–14:00. On the other hand, $nL_w(660)$ in the offshore plume of the ECS were notably lower at 14:00 in the afternoon than those at about 10:00 in the morning. Similarly, $K_d(490)$ in the plume region were also observed to drop significantly from 10:00–15:00 (Fig. 10z–10ee).

3.3.2. A summer day example

Fig. 11 shows the diurnal variabilities on a summer day of August 16, 2019. In comparison to $nL_w(\lambda)$ and $K_d(490)$ in a winter day (Fig. 10) and a spring day (Fig. 7), the coastal region in the YS and ECS featured less turbid waters. For $nL_w(443)$ (Fig. 11a–11h) and $nL_w(555)$ (Fig. 11i–11p), the diurnal variations were less significant for both open oceans and coastal regions. Values of $nL_w(660)$ and $K_d(490)$, as well as the coverage area of the enhanced $nL_w(660)$ and $K_d(490)$, were less than those on the winter- and spring-day. This is consistent with the result from a previous study (Shi and Wang, 2014). Indeed, diurnal variations of $nL_w(660)$ (Fig. 11q–11x) and $K_d(490)$ (Fig. 11y–11ff) along the coastal region of the YS and ECS were remarkable from 09:00–16:00. Specifically, the region with $nL_w(660) > \sim5$ mW cm^{-2} μm^{-1} sr^{-1} accounted for a large portion of the Subei Shoal region in the YS at 09:00 (Fig. 11q). It gradually shrank to a smaller portion in the region at 14:00 (Fig. 11v). Similarly, the extremely turbid coastal region with $K_d(490) > \sim3$ m^{-1} also decreased significantly from 09:00–14:00 in the YS (Fig. 11y–11dd).

3.3.3. An autumn day example

On the autumn day of November 15, 2019, GOCI-measured $nL_w(\lambda)$ and $K_d(490)$ (Fig. 12) showed less diurnal variabilities than those in the other three season days (Figs. 7, 10, and 11). It is noted that, as shown in Fig. 12, there were few ocean color retrievals at 16:00 on that autumn day, primarily due to cases of high solar-zenith angles. For $nL_w(443)$ (Fig. 12a–12h) and $nL_w(555)$ (Fig. 12i–12p), both their spatial patterns and magnitudes were similar for the seven GOCI shots from 09:00–15:00. However, some small diurnal changes could still be observed from the seven GOCI shots of $nL_w(660)$ (Fig. 12q–12w) and $K_d(490)$ (Fig. 12y–12ee). From 09:00–12:00, the coverage of highly
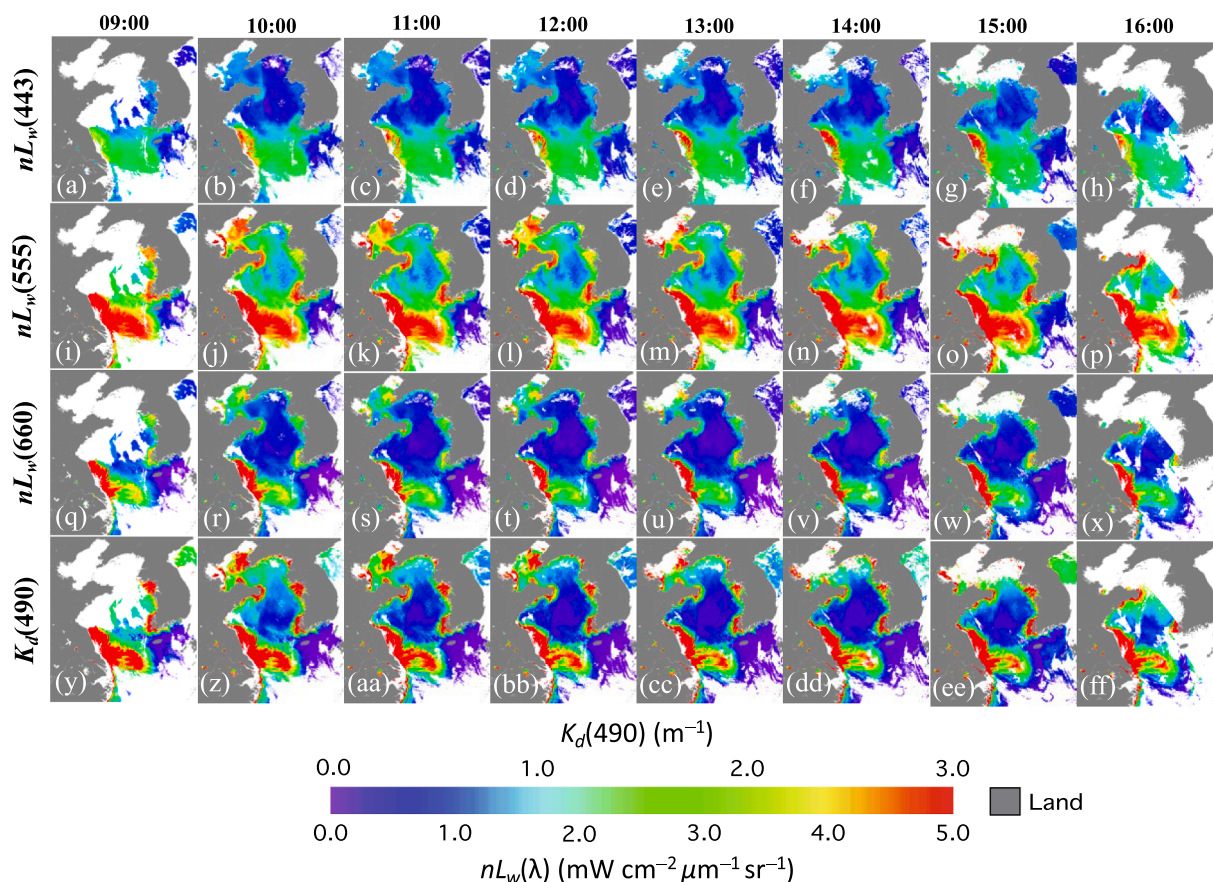

Fig. 10. GOCI ocean color retrievals at local times of 09:00–16:00 on January 24, 2019, in the BS, YS, and ECS for (a–h) $nL_w(443)$, (i–p) $nL_w(555)$, (q–x) $nL_w(660)$, and (y–ff) $K_d(490)$.
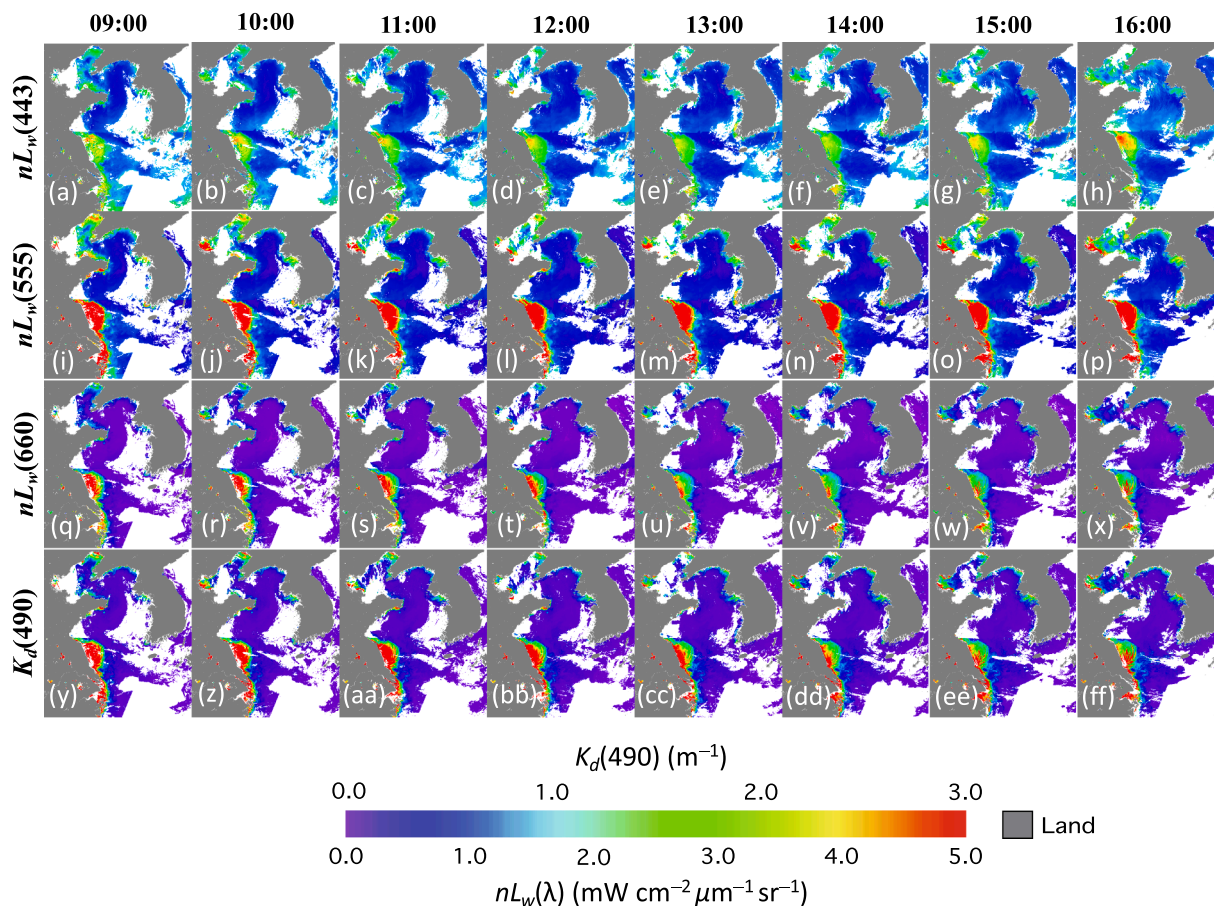
Fig. 11. GOCI ocean color retrievals at local times of 09:00–16:00 on August 16, 2019, in the BS, YS, and ECS for (a–h) $nL_w(443)$, (i–p) $nL_w(555)$, (q–x) $nL_w(660)$, and (y–ff) $K_d(490)$.

turbid waters with $nL_w(660) > \sim 5$ mW cm^{-2} μm^{-1} sr^{-1} and $K_d(490) > \sim 3$ m^{-1} decreased slightly in the coastal region along the YS and ECS. The size of the offshore plume in the ECS also contracted slightly between 09:00 and 12:00. Correspondingly, $nL_w(660)$ and $K_d(490)$ values dropped in the offshore sediment plume and coastal turbid waters. After 12:00, the coverage of highly turbid waters and the area of sediment plume were further expanded as shown in Fig. 12u–12w and Fig. 12cc–12ee.

3.3.4. Quantitative evaluations and analyses

Figs. 10–12 show variability of $nL_w(\lambda)$ and $K_d(490)$ spatial distributions in different seasons in the BS, YS, and ECS. To further quantify the diurnal variability of $nL_w(\lambda)$ and $K_d(490)$, GOCI measurements at stations A and B (marked in Fig. 5a) are analyzed. These two stations can adequately represent the near-shore and the offshore waters in the region.

3.3.4.1. Evaluations at station A. On January 24, 2019, $nL_w(\lambda)$ spectra showed monotonous declines from 10:00–14:00 at location A (Fig. 13a). In fact, $nL_w(412)$, $nL_w(443)$, $nL_w(490)$, and $nL_w(555)$ increased slightly from 09:00–10:00 and then declined moderately from 10:00–14:00, while drops were more significant for $nL_w(660)$ and $nL_w(680)$ from 09:00–15:00. Specifically for $nL_w(443)$, it was ~ 3.1 mW cm^{-2} μm^{-1} sr^{-1} at 09:00, increased to ~ 3.8 mW cm^{-2} μm^{-1} sr^{-1} at 10:00, and then decreased to the lowest ~ 2.6 mW cm^{-2} μm^{-1} sr^{-1} at 15:00 on that day. On the other hand, $nL_w(680)$ was ~ 5.8 mW cm^{-2} μm^{-1} sr^{-1} at 09:00, became the lowest of ~ 1.9 mW cm^{-2} μm^{-1} sr^{-1} at 15:00, and then increased to ~ 2.7 mW cm^{-2} μm^{-1} sr^{-1} at 16:00. The change of $nL_w(\lambda)$ in these eight GOCI shots was consistent with $nL_w(\lambda)$ spatial distributions as shown in Fig. 7. In fact, the large drops of $nL_w(555)$, $nL_w(660)$, and $nL_w(680)$ reflected the effect of the front movement on the highly turbid waters.

We note that the NIR $nL_w(745)$ at station A (Fig. 13a) were quite significant about 2.4, 2.4, 2.2, 1.6, 0.71, 0.36, 0.43, and 0.89 mW cm^{-2} μm^{-1} sr^{-1} at hourly from 09:00–16:00, respectively. This shows that oceans in the region were not black at the NIR bands, thus a regional-specific atmospheric correction algorithm is necessary to derive ocean color data accurately (Wang et al., 2013a; Wang et al., 2012). Correspondingly, Fig. 13g shows that $K_d(490)$ dropped from ~ 4.7 m^{-1} at 09:00 to the lowest daily value of ~ 1.4 m^{-1} at 15:00, and then increased slightly to ~ 1.9 m^{-1} at 16:00. It is expected that over such highly turbid waters the other ocean property products, e.g., SPM, inherent optical properties (IOPs), etc., also had the similar diurnal changes.

On the summer day of August 16, 2019, GOCI-derived $nL_w(\lambda)$ spectra at station A showed moderate change from 09:00–16:00 (Fig. 13c). The peak $nL_w(\lambda)$ occurred at 09:00 for all GOCI bands, and the lowest $nL_w(\lambda)$ occurred between 13:00 and 14:00. For $nL_w(\lambda)$ at 412, 443, 490, and 555 nm, the diurnal variations from 09:00–16:00 were less than ~ 1.0 mW cm^{-2} μm^{-1} sr^{-1}. In comparison, $nL_w(660)$ and $nL_w(680)$ dropped from ~ 3.5 mW cm^{-2} μm^{-1} sr^{-1} at 09:00 to ~ 1.5 mW cm^{-2} μm^{-1} sr^{-1} at 14:00. At station A, $nL_w(745)$ were in the range between ~ 0.2 and ~ 0.6 mW cm^{-2} μm^{-1} sr^{-1}, which were much less than those during the winter season (but still significant). At this station, $K_d(490)$ changed from ~ 3.0 m^{-1} at 09:00 to the lowest of ~ 1.5 m^{-1} at 14:00, and increased to $> \sim 2.5$ m^{-1} at 16:00 (Fig. 13g). The diurnal variability of $K_d(490)$ agreed well with the change of $K_d(490)$ spatial distribution from 09:00–16:00 (Fig. 11y–11ff).

On the autumn day of November 15, 2019, GOCI-measured $nL_w(\lambda)$ spectra at station A showed the least diurnal variability in the four daily
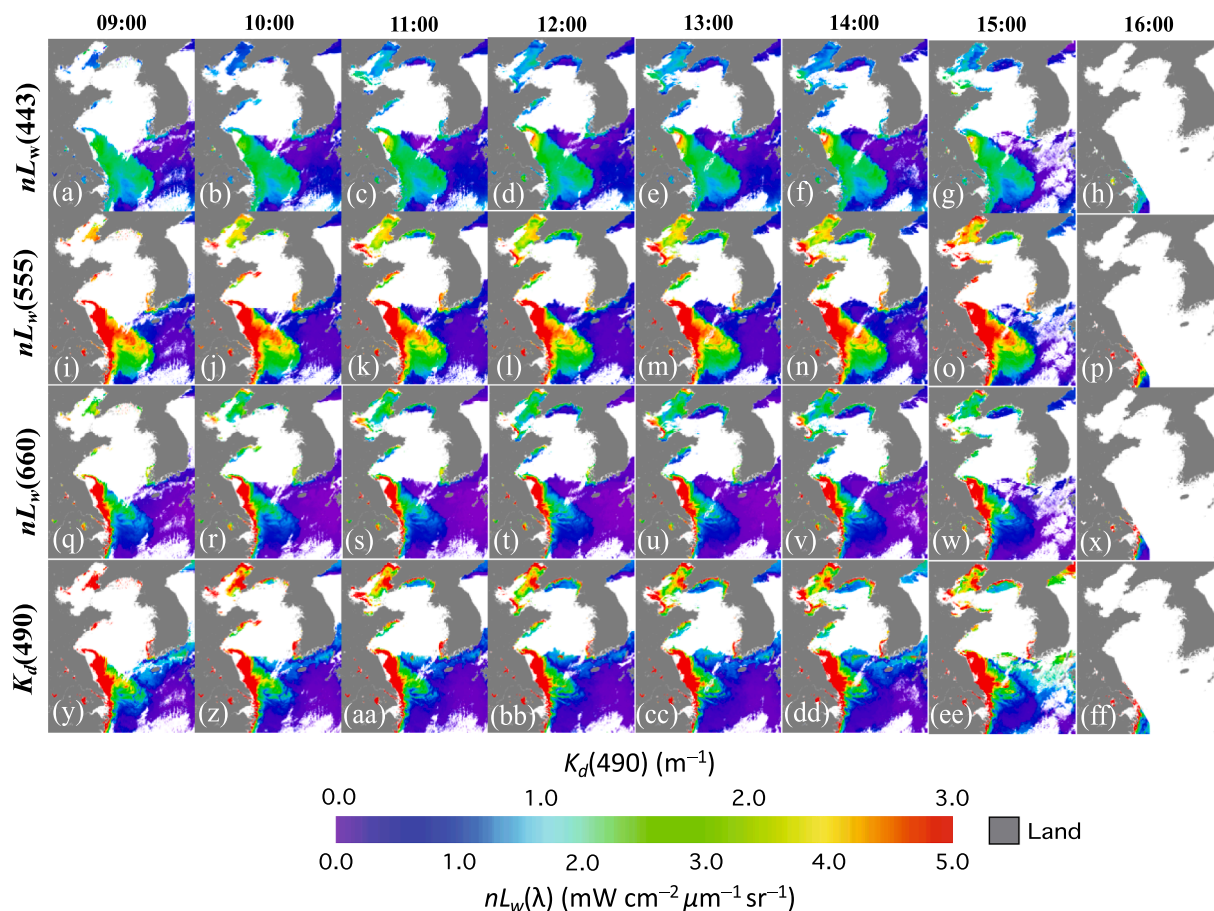
Fig. 12. GOCI ocean color retrievals at around local times of 09:00–16:00 on November 15, 2019, in the BS, YS, and ECS for (a–h) $nL_w(443)$, (i–p) $nL_w(555)$, (q–x) $nL_w(660)$, and (y–ff) $K_d(490)$.

examples from four different seasons (Fig. 13e). Indeed, as shown in Fig. 13e, $nL_w(\lambda)$ at 412, 443, and 490 nm displayed little diurnal variation from 09:00–14:00 (relatively flat). However, the diurnal variation of $nL_w(\lambda)$ at GOCI red bands 660 and 680 nm were still discernable with $nL_w(660)$ and $nL_w(680)$ of ~3.4 and ~3.1 mW cm^{-2} μm^{-1} sr^{-1} at 09:00, decreased to ~2.3 and ~2.0 mW cm^{-2} μm^{-1} sr^{-1} at 12:00, and then increased to ~2.9 and ~2.6 mW cm^{-2} μm^{-1} sr^{-1} at 15:00 (Fig. 13e). On November 15, 2019, the NIR $nL_w(745)$ were also significant as values changed from ~0.73 mW cm^{-2} μm^{-1} sr^{-1} at 09:00 to ~0.38 mW cm^{-2} μm^{-1} sr^{-1} at 12:00, and then increased to ~0.51 mW cm^{-2} μm^{-1} sr^{-1} at 15:00. Correspondingly, $K_d(490)$ was ~3.2 m^{-1} at 09:00, it dropped to ~2.0 m^{-1} at 12:00, and then gradually increased to 2.7 m^{-1} again at 15:00 (Fig. 13g). It is also noted that the diurnal variabilities of $nL_w(\lambda)$ and $K_d(490)$ at station A are representative for the China's east coastal region. In fact, the diurnal variabilities of $nL_w(\lambda)$ and $K_d(490)$ at station D in the BS are similar to those at station A, while the diurnal variability at station C is usually insignificant.

3.3.4.2. Evaluations at station B. In comparison with results at station A, the diurnal variability of $nL_w(\lambda)$ and $K_d(490)$ at station B (Fig. 13b, 13d, 13f, and 13h) were less significant. In addition, the diurnal variabilities of $nL_w(\lambda)$ and $K_d(490)$ between stations A and B were not in phase for the three days of GOCI observations. On January 24, 2019, the diurnal variabilities of $nL_w(\lambda)$ at all the GOCI bands were small with the biggest change at the two red bands (Fig. 13b). $nL_w(680)$ dropped by ~0.9 mW cm^{-2} μm^{-1} sr^{-1} from ~4.0 mW cm^{-2} μm^{-1} sr^{-1} at 09:00 to ~3.1 mW cm^{-2} μm^{-1} sr^{-1} at 14:00 (Fig. 13b). In comparison, $nL_w(680)$ dropped from ~5.8 mW cm^{-2} μm^{-1} sr^{-1} at 09:00 to ~1.9 mW cm^{-2} μm^{-1} sr^{-1} at 15:00 at station A on the same day. Similarly, $K_d(490)$ only dropped

from ~3.6 m^{-1} to ~2.9 m^{-1} at station B in the same time frame (Fig. 13h).

On August 16, 2019, the water type at station B was typical clear open ocean with enhanced $nL_w(\lambda)$ at the blue bands (Fig. 13d). The biggest hourly $nL_w(\lambda)$ changes occurred between 09:00–11:00 as $nL_w(443)$ dropped from ~1.7 mW cm^{-2} μm^{-1} sr^{-1} to ~0.7 mW cm^{-2} μm^{-1} sr^{-1} (Fig. 13d). In this period, $K_d(490)$ increased from ~0.08 m^{-1} to ~0.11 m^{-1} (Fig. 13h). However, from 12:00 to 16:00, the changes of $nL_w(\lambda)$ and $K_d(490)$ were limited. Comparisons of the diurnal variabilities of $nL_w(\lambda)$ and $K_d(490)$ at these two stations (A and B) provide clear evidences for their differences both in magnitudes and their phases.

On November 15, 2019, $nL_w(\lambda)$ and $K_d(490)$ at station B show little variability at the short-blue/blue bands of 412 and 443 nm from 09:00–15:00 (Fig. 13f). For the red band at 660 nm, $nL_w(660)$ dropped from ~1.9 mW cm^{-2} μm^{-1} sr^{-1} at 09:00 to ~1.1 mW cm^{-2} μm^{-1} sr^{-1} at 14:00 (Fig. 13f), while $K_d(490)$ decreased from ~1.7 m^{-1} to ~0.7 m^{-1}, correspondingly (Fig. 13h). From 14:00 to 15:00, $nL_w(660)$ increased to ~1.3 m^{-1} and $K_d(490)$ changed to ~1.2 m^{-1} (Fig. 13f and 13 h).

3.3.5. Characterize seasonal $K_d(490)$ diurnal variability

Figs. 7, 10, 11, and 12 show examples of the diurnal variability in $nL_w(\lambda)$ and $K_d(490)$ from 09:00–16:00 in the four seasons in the region. To further characterize and quantify the seasonality difference of diurnal variability, we computed the hourly climatology $K_d(490)$ from 09:00–16:00 in January (winter), April (spring), July (summer), and October (autumn) using the GOCI observations from 2011–2020. Fig. 14 shows that the seasonal change of diurnal variability in these four months is significant. In general, $K_d(490)$ in the coastal regions of the BS, YS, and ECS are greatly enhanced in terms of $K_d(490)$ magnitude and
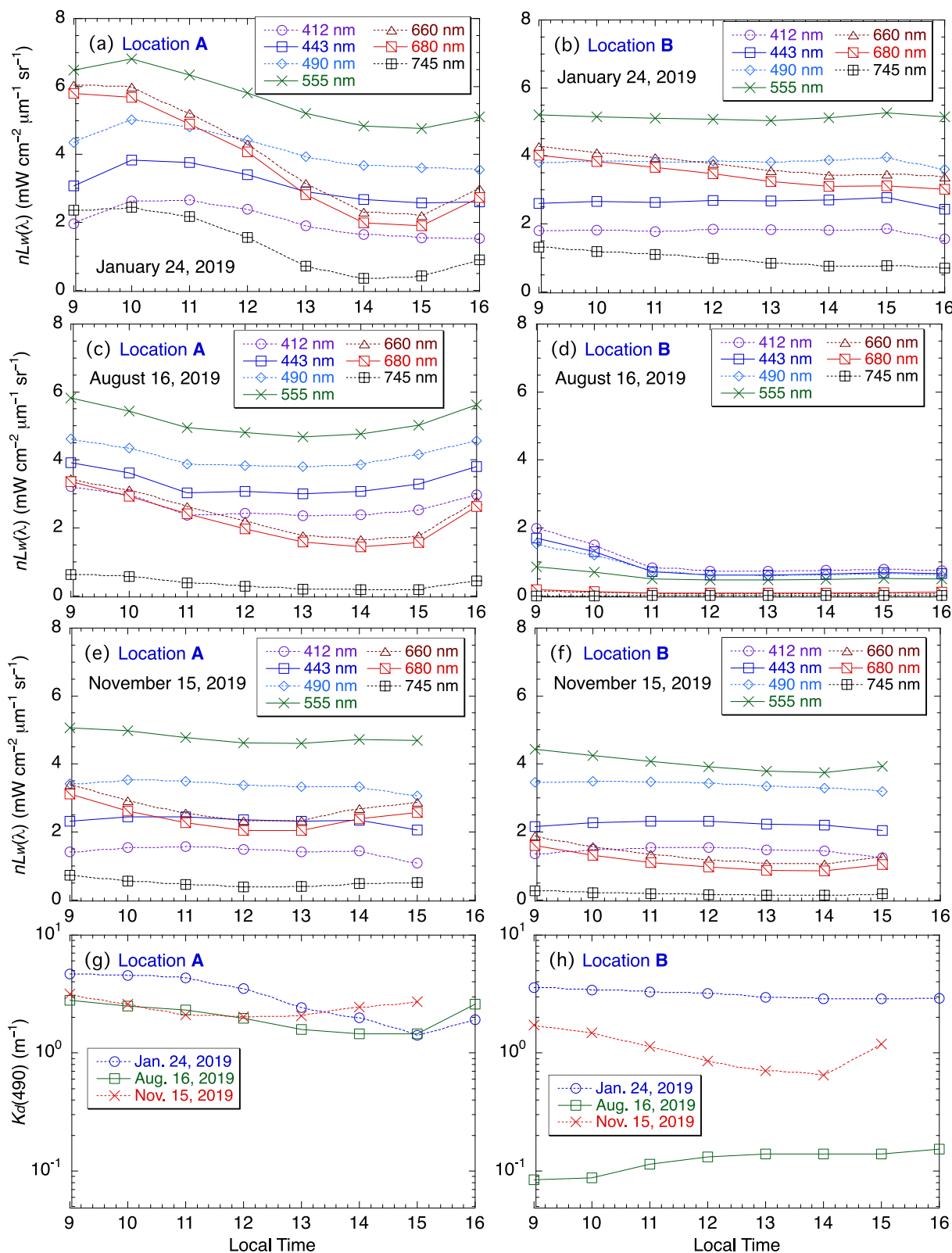
Fig. 13. Diurnal variations of $nL_w(\lambda)$ at stations A and B in the three days (corresponding to three different seasons) on (a and b) January 24, 2019, (c and d) August 16, 2019, and (e and f) November 15, 2019. Plots g and h show the diurnal variation of the corresponding $K_d(490)$ at stations A and B on these three days.

high $K_d(490)$ coverage in January (Fig. 14a–14h), while it is significantly reduced in the summer season (July) (Fig. 14q–14x). This reflects the seasonal variability of $K_d(490)$ in the region (Shi and Wang, 2012, 2014). It is also noted that at 09:00 (Fig. 14a) and 16:00 (Fig. 14h) in January, there are large areas without any valid $K_d(490)$ data due to

large solar-zenith angles (>70°).

In each season, the $K_d(490)$ diurnal variability is also noticeable from 09:00–16:00 although the variation is not as significant as the seasonal variability. In the BS, the area with $K_d(490) > 3 \text{ m}^{-1}$ continuously drops from 10:00 until around 14:00–15:00 in the afternoon, and the area with
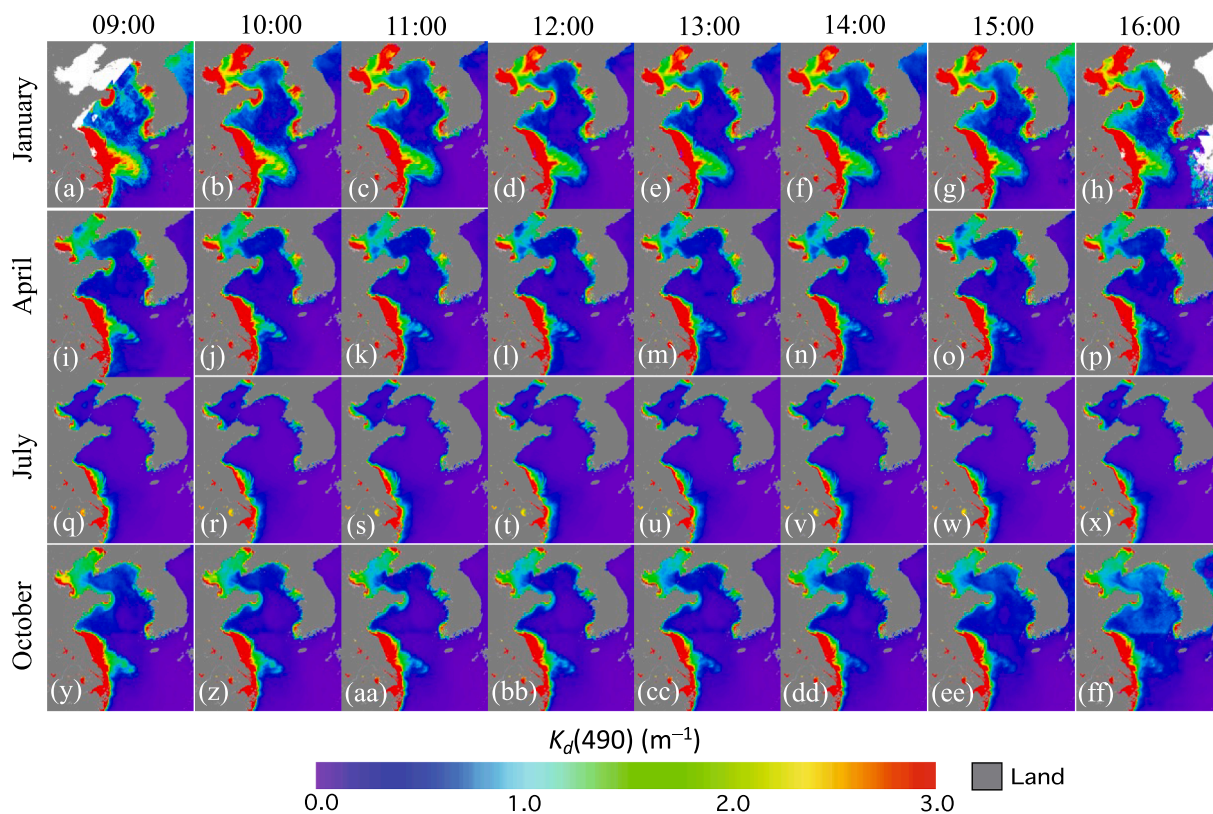
Fig. 14. Hourly GOCI-derived climatology in $K_d(490)$ from the local time of 09:00–16:00 for the month (season) of (a–h) January (winter), (i–p) April (spring), (q–x) July (summer), and (y–ff) October (autumn).

$K_d(490) > 3$ m^{-1} at 16:00 further expands around 14:00–15:00. A similar diurnal trend of $K_d(490)$ in the BS can also be found in October (Fig. 14y–14ff). In the ECS, $K_d(490)$ in the offshore sediment plume is the highest at 09:00 in all four seasons. $K_d(490)$ gradually drops until around 14:00–15:00 and begins to increase at 16:00. An analogous diurnal trend of the enhanced $K_d(490)$ can also be found in the four seasons, especially in January (Fig. 14a–14 h), April (Fig. 14i–14p), and October (Fig. 14y–14ff).

Table 6 further quantifies the hourly climatology $K_d(490)$ (mean values) from 09:00–16:00 at stations A, B, C, and D. Clearly, the climatology diurnal variability at these four stations is considerably different. At station A, the diurnal change in $K_d(490)$ is significant, and

the lowest $K_d(490)$ occurs at around 13:00 for all the four seasons, while the peak $K_d(490)$ is normally at ~09:00. However, for January, the peak $K_d(490)$ is also at ~16:00. At station B, the magnitude of $K_d(490)$ is lower than that at station A, even though the diurnal variation in $K_d(490)$ is similar. In the open ocean at station C, $K_d(490)$ values keep stable with little diurnal changes from 09:00–16:00 in all the four seasons. At statin D in the BS, $K_d(490)$ range between ~3.3 m^{-1} and ~4.0 m^{-1} in January, while diurnal variations in $K_d(490)$ are less significant for other three months. In particular, in summer time there is essentially no diurnal variation in $K_d(490)$ at station D (with also significantly low $K_d(490)$ values). Results in Fig. 14 and Table 6 suggest that the diurnal variation in $K_d(490)$ is regional-dependent due to different physical,

Table 6
Mean $K_d(490)$ at stations of A, B, C, and D (noted in Fig. 5a) from monthly climatology $K_d(490)$ results in Fig. 14 for GOCI eight shots from 09:00–16:00 and for four months in January, April, July, and October.

Month	Station	Mean $K_d(490)$* at Time							
		09:00	10:00	11:00	12:00	13:00	14:00	15:00	16:00
January	A	4.35	4.16	3.94	3.89	3.87	3.96	4.13	4.48
	B	—	3.49	3.34	3.27	3.30	3.43	3.53	3.93
	C	0.05	0.06	0.05	0.06	0.06	0.05	0.06	0.06
	D	—	3.49	3.34	3.27	3.30	3.43	3.53	3.93
April	A	3.24	3.08	2.84	2.62	2.71	2.77	2.91	2.99
	B	1.85	1.69	1.67	1.57	1.52	1.50	1.52	1.59
	C	0.05	0.05	0.06	0.05	0.05	0.06	0.06	0.06
	D	1.85	1.69	1.67	1.57	1.52	1.50	1.52	1.59
July	A	0.75	0.72	0.64	0.62	0.56	0.55	0.59	0.60
	B	0.19	0.19	0.20	0.20	0.21	0.21	0.20	0.20
	C	0.05	0.05	0.05	0.05	0.05	0.05	0.05	0.05
	D	0.19	0.19	0.20	0.20	0.21	0.21	0.20	0.20
October	A	3.16	2.76	2.47	2.15	2.00	1.97	2.24	2.52
	B	1.56	1.34	1.25	1.19	1.12	1.08	1.11	1.19
	C	0.05	0.05	0.05	0.05	0.05	0.05	0.05	0.06
	D	1.56	1.34	1.25	1.19	1.12	1.08	1.11	1.19

*Unit: m^{-1} for $K_d(490)$.

optical, biological, and biogeochemical water properties and their processes. It should also be noted again that, except for station C in open oceans, seasonal variations in $K_d(490)$ are usually much more significant than those of the diurnal changes in the region as shown in Fig. 14 and Table 6.

4. Discussions and conclusion

As one of the most dynamic and complicated waters in world oceans, the atmospheric and atmosphere-ocean interaction processes, and the ocean physical and biological processes are the major driving forces for the diurnal variability in the western Pacific region (He et al., 2013; Wang et al., 2013a; Wu et al., 2022). Seasonal variabilities of ocean properties are attributed to seasonal winds, ocean layer stratification, and ocean thermodynamics, as well as ocean bathymetry and river discharges. The spring-neap tidal effects (in a lunar cycle of 29.53 days) on the variations of GOCI-derived ocean color property is in the same order as the seasonal variations (Shi et al., 2011).

At the ocean diurnal scale, it has already been found that the diurnal variation of the land-ocean breeze effect is significant (Chen et al., 2016). In this study, we use hourly climatology $K_d(490)$ from the GOCI measurements from 2011 to 2020 to further characterize the seasonality of the diurnal variability in the water turbidity. Although the $K_d(490)$ diurnal variability in four seasons is generally less significant than their seasonal component, the $K_d(490)$ diurnal variability is not negligible. It is noted that the land-ocean breeze effect, i.e., the diurnal change of wind as reported in Chen et al. (2016), may contribute to the climatology $K_d(490)$ diurnal variability shown in Fig. 14 and Table 6.

There exist large tides and strong tidal currents in the broad continental shelf of the ECS (Bao et al., 2001; Larsen et al., 1985). The diurnal and semidiurnal internal tides show distinct variability along the ECS shelf (Wang et al., 2022). In the Hangzhou Bay region, it has been found that there was an increasing trend of SPM at the ebb tide with an increase of ~3.96±0.31 mg/L/min mainly due to re-suspension of SPM particles driven by the tide change (Chen et al., 2021). In the region of the Hangzhou Bay and Yangtze River Estuary, the diurnal changes of SPM were also observed from VIIRS Day/Night measurements (Shi and Wang, 2018). All these studies suggest that diurnal ocean dynamics in the GOCI-covered region is strong, and polar-orbiting satellites may not be able to effectively monitor the diurnal variability in the marginal western Pacific oceans. Therefore, GOCI observations indeed provide important data to study the ocean optical, biological, and ecological processes more completely.

To confirm GOCI ocean color data quality and due to unavailable of in situ data in recent years, the GOCI-measured $nL_w(\lambda)$ and $K_d(490)$ are compared with those of VIIRS in 2012, 2016, and 2019, demonstrating generally consistent results (within ~5–10%). Therefore, using the GOCI-derived ocean color products in 2012 as a reference to relate to the Wang et al. (2013a) validation results, we show that GOCI-derived $nL_w(\lambda)$ and $K_d(490)$ data are reasonable in 2019, and can be reliably used in the study. This also shows that in this period the GOCI sensor on orbital performance has been reasonably well characterized.

We use GOCI measurements from 2019 and compare the availability of ocean color retrievals to the corresponding data coverage from VIIRS. The statistical results show that the daily coverage of valid retrievals increases from ~21.77% from VIIRS to ~43.81% from GOCI measurements. For most of data in 2019, the daily valid GOCI retrievals increase by about a factor of two, compared with that from VIIRS. In addition, using the GOCI daily data as an example, we demonstrate that GOCI observations can provide significant improvement of the ocean color data coverage. Furthermore, it has also shown that the optimal ocean color data coverage in the region from satellite remote sensing is around 10:00–11:00 and 12:00–13:00, corresponding to preferred morning and afternoon satellite orbitals.

We have used STDs and CVs from the daily GOCI eight measurements to provide examples of quantifying ocean diurnal variations for various locations representing different water properties. Results show that, over turbid coastal waters, $STD[nL_w(\lambda)]$ and $CV[nL_w(\lambda)]$ at the green and red (even at the NIR) bands are useful, while for open oceans STD $[nL_w(\lambda)]$ and $CV[nL_w(\lambda)]$ at the short-blue/blue and green bands are important. $STD[K_d(490)]$ and $CV[K_d(490)]$ can also provide useful information and are generally consistent with results from $STD[nL_w(\lambda)]$ and $CV[nL_w(\lambda)]$. Therefore, daily STD and CV measurements can provide quantitative information of the regional ocean/water diurnal variations.

Some advantages of GOCI data, e.g., more cloud-free daily data and the capability of hourly monitoring of ocean variability, demonstrate that the GEO satellite observations for coastal oceans and inland lakes are important for addressing and understanding of various ocean/water processes associated with their diurnal variabilities. Therefore, using the GEO ocean color measurements, we can better monitor and study the regional ocean environmental changes over inshore and offshore waters, riverine estuaries of continental shelf, and various atmosphere-ocean processes.

Declaration of Competing Interest

The authors declare that they have no known competing financial interests or personal relationships that could have appeared to influence the work reported in this paper.

Data availability

Data will be made available on request.

References

Bao, X., Gao, G., Yan, J.u., 2001. Three dimensional simulation of tide and tidal current characteristics in the East China Sea. Oceanol. Acta 24 (2), 135–149.

Barnes, B.B., Cannizzaro, J.P., English, D.C., Hu, C., 2019. Validation of VIIRS and MODIS reflectance data in coastal and oceanic waters: An assessment of methods. Remote Sens. Environ. 220, 110–123.

Bi, N., Yang, Z., Wang, H., Fan, D., Sun, X., Lei, K., 2011. Seasonal variation of suspended-sediment transport through the southern Bohai Strait. Estuar. Coast. Shelf Sci. 93 (3), 239–247.

Chen, X.C., Zhang, F.Q., Zhao, K., 2016. Diurnal Variations of the Land-Sea Breeze and Its Related Precipitation over South China. J. Atmos. Sci. 73, 4793–4815.

Chen, Q., Zhou, B., Yu, Z., Wu, J., Tang, S., 2021. Detection of the Minute Variations of Total Suspended Matter in Strong Tidal Waters Based on GaoFen-4 Satellite Data. Remote Sens. 13 (7), 1339. https://doi.org/10.3390/rs13071339.

Cheng, Z., Wang, X.H., Paull, D., Gao, J., 2016. Application of the geostationary ocean color imager to mapping the diurnal and seasonal variability of surface suspended matter in a macro-tidal estuary. Remote Sens 8, 244. https://doi.org/10.3390/rs8030244.

Choi, W.J., Moon, K.-J., Yoon, J., Cho, A., Kim, S.-k., Lee, S., Ko, D.h., Kim, J., Ahn, M.H., Kim, D.-R., Kim, S.-M., Kim, J.-Y., Nicks, D., Kim, J.-S., 2018. Introducing the geostationary environment monitoring spectrometer. Journal of Applied Remote Sensing 12, 044005. https://doi.org/10.1117/1.JRS.12.044005.

Choi, J.-K., Park, Y.J., Ahn, J.H., Lim, H.-S., Eom, J., Ryu, J.-H., 2012. GOCI, the world's first geostationary ocean color observation satellite, for the monitoring of temporal variability in coastal water turbidity. J. Geophys. Res. 117, C09004. https://doi.org/10.1029/2012JC008046.

Choi, J.-K., Min, J.-E., Noh, J.H., Han, T.-H., Yoon, S., Park, Y.J., Moon, J.-E., Ahn, J.-H., Ahn, S.M., Park, J.-H., 2014. Harmful algal bloom (HAB) in the East Sea identified by the Geostationary Ocean Color Imager (GOCI). Harmful Algae 39, 295–302.

Concha, J., Mannino, A., Franz, B., Kim, W., 2019. Uncertainties in the Geostationary Ocean Color Imager (GOCI) remote sensing reflectance for assessing diurnal variability of biogeochemical processes. Remote Sens. 11, 295. https://doi.org/10.3390/rs11030295.

Dong, L.X., Guan, W.B., Chen, Q., Li, X.H., Liu, X.H., Zeng, X.M., 2011. Sediment transport in the Yellow Sea and East China Sea. Estuar. Coast. Shelf Sci. 93 (3), 248–258.

Doxaran, D., Lamquin, N., Park, Y.J., Mazeran, C., Ryu, J.H., Wang, M., Poteau, A., 2014. Retrieval of the seawater reflectance for suspended solids monitoring in the East China Sea using MODIS, MERIS and GOCI satellite data. Remote Sens. Environ. 146, 36–48.

Fishman, J., Iraci, L.T., Al-Saadi, J., Chance, K., Chavez, F., Chin, M., Coble, P., Davis, C., DiGiacomo, P.M., Eldering, A., Edwards, D., Goes, J., Herman, J., Hu, C., Jacob, D., Jordan, C., Kawa, S.R., Key, R., Liu, X., Lohrenz, S., Mannino, A., Natrai, V., Neil, D., Neu, J., Newchurch, M., Pickering, K., Salisbury, J., Sosik, H., Subramaniam, A., Tzortziou, M., Wang, J., Wang, M., 2012. The United States' next generation of atmospheric composition and coastal ecosystem measurements: NASA's geostationary coastal and air pollution events (GEO-CAPE) mission. Bull. Amer. Meteor. Soc. 93, 1547–1566.

Goldberg, M.D., Kilcoyne, H., Cikanek, H., Mehta, A., 2013. Joint Polar Satellite System: The United States next generation civilian polar-orbiting environmental satellite system. J. Geophys. Res. Atmos. 118 (24), 13,463–13,475.

Gordon, H.R., Clark, D.K., Mueller, J.L., Hovis, W.A., 1980. Phytoplankton Pigments from the Nimbus-7 Coastal Zone Color Scanner: Comparisons with Surface Measurements. Science 210 (4465), 63–66.

Gordon, H.R., Wang, M., 1994. Retrieval of water-leaving radiance and aerosol optical thickness over the oceans with SeaWiFS: A preliminary algorithm. Appl. Opt. 33, 443–452.

He, X., Bai, Y., Pan, D., Huang, N., Dong, X., Chen, J., Chen, C.-T.-A., Cui, Q., 2013. Using geostationary satellite ocean color data to map the diurnal dynamics of suspended particulate matter in coastal waters. Remote Sens. Environ. 133, 225–239.

Hovis, W.A., Clark, D.K., Anderson, F., Austin, R.W., Wilson, W.H., Baker, E.T., Ball, D., Gordon, H.R., Mueller, J.L., El-Sayed, S.Z., Sturm, B., Wrigley, R.C., Yentsch, C.S., 1980. Nimbus-7 Coastal Zone Color Scanner - System Description and Initial Imagery. Science 210 (4465), 60–63.

Huang, C., Yang, H., Zhu, A.-X., Zhang, M., Lü, H., Huang, T., Zou, J., Li, Y., 2015. Evaluation of the Geostationary Ocean Color Imager (GOCI) to monitor the dynamic characteristics of suspension sediment in Taihu Lake. Int. J. Remote Sens. 36 (15), 3859–3874.

IOCCG, 2010. Atmospheric Correction for Remotely-Sensed Ocean-Colour Products, Wang, M. (Ed.), In: Reports of the International Ocean-Colour Coordinating Group, No. 10. IOCCG, Dartmouth, Canada. https://doi.org/10.25607/OBP-101.

IOCCG, 2012. Ocean-Colour Observations From a Geostationary Orbit, Antoine, D. (Ed.), In: Reports of the International Ocean-Colour Coordinating Group, No. 12. IOCCG, Dartmouth, Canada. https://doi.org/10.25607/OBP-103.

Jiang, L., Wang, M., 2013. Identification of pixels with stray light and cloud shadow contaminations in the satellite ocean color data processing. Appl. Opt. 52, 6757–6770.

Jiang, L., Wang, M., 2014. Improved near-infrared ocean reflectance correction algorithm for satellite ocean color data processing. Opt. Express 22, 21657–21678.

Jiang, L., Wang, M., 2017. Ocean diurnal currents in the Bohai Sea derived from the Korean Geostationary Ocean Color Imager. IEEE Trans. Geosci. Remote Sens. 55 (3), 1437–1450.

Kim, D., Park, M.-S., Park, Y.-J., Kim, W., 2020. Geostationary Ocean Color Imager (GOCI) marine fog detection in combination with Himawari-8 based on the decision tree. Remote Sens. 12, 149. https://doi.org/10.3390/rs12010149.

Larsen, L.H., Cannon, G.A., Choi, B.H., 1985. East Chia Sea tide currents. Cont. Shelf Res. 4, 77–103.

Liu, J., Liu, J., He, X., Pan, D., Bai, Y., Zhu, F., Chen, T., Wang, Y., 2018. Diurnal dynamics and seasonal variations of total suspended particulate matter in highly turbid hangzhou bay waters based on the geostationary ocean color imager. IEEE J. Sel. Top. Appl. Earth Obs. Remote Sens. 11 (7), 2170–2180.

Liu, X., Wang, M., 2016. Analysis of diurnal variations from the Korean Geostationary Ocean Color Imager measurements using the DINEOF method. Estuar. Coast. Shelf Sci. 180, 230–241. https://doi.org/10.1016/ecss.2016.07.006.

Lou, X., Hu, C., 2014. Diurnal changes of a harmful algal bloom in the East China Sea: Observations from GOCI. Remote Sens. Environ. 140, 562–572.

Mikelsons, K., Wang, M., 2019. Optimal satellite orbit configuration for global ocean color product coverage. Opt. Express 27, A445–A457.

Mikelsons, K., Wang, M., Jiang, L., 2020. Statistical evaluation of satellite ocean color data retrievals. Remote Sens. Environ. 237, 111601. https://doi.org/10.1016/j.rse.2019.111601.

Mueller, J.L., 2000. SeaWiFS algorithm for the diffuse attenuation coefficient, K(490), using water-leaving radiances at 490 and 555 nm. NASA Goddard Space Flight Center, Greenbelt, Maryland, pp. 24–27.

Park, M.-S., Lee, S., Ahn, J.-H., Lee, S.-J., Choi, J.-K., Ryu, J.-H., 2022. Decadal Measurements of the First Geostationary Ocean Color Satellite (GOCI) Compared with MODIS and VIIRS Data. Remote Sens. 14, 72. https://doi.org/10.3390/rs14010072.

Ryu, J.-H., Han, H.-J., Cho, S., Park, Y.-J., Ahn, Y.-H., 2012. Overview of geostationary ocean color imager (GOCI) and GOCI data processing system (GDPS). Ocean Science Journal 47 (3), 223–233.

Shi, W., Wang, M., 2012. Satellite views of the Bohai Sea, Yellow Sea, and East China Sea. Prog. Oceanogr. 104, 30–45.

Shi, W., Wang, M., 2014. Ocean reflectance spectra at the red, near-infrared, and shortwave infrared from highly turbid waters: A study in the Bohai Sea, Yellow Sea, and East China Sea. Limnol. Oceanogr. 59 (2), 427–444.

Shi, W., Wang, M., 2018. Ocean dynamics observed by VIIRS day/night band satellite observations. Remote Sens. 10, 76. https://doi.org/10.3390/rs10010076.

Shi, W., Wang, M., Jiang, L., 2011. Spring-neap tidal effects on satellite ocean color observations in the Bohai Sea, Yellow Sea, and East China Sea. J. Geophys. Res. 116, C12932. https://doi.org/10.1029/2011JC007234.

Sun, J., Wang, M., 2015. Radiometric calibration of the VIIRS reflective solar bands with robust characterizations and hybrid calibration coefficients. Appl. Opt. 54, 9331–9342.

Wang, M., 1999. A sensitivity study of SeaWiFS atmospheric correction algorithm: Effects of spectral band variations. Remote Sens. Environ. 67, 348–359.

Wang, M., 2007. Remote sensing of the ocean contributions from ultraviolet to near-infrared using the shortwave infrared bands: simulations. Appl. Opt. 46, 1535–1547.

Wang, M., Isaacman, A., Franz, B.A., McClain, C.R., 2002. Ocean color optical property data derived from the Japanese Ocean Color and Temperature Scanner and the French Polarization and Directionality of the Earth's Reflectances: A comparison study. Appl. Opt. 41, 974–990.

Wang, M., Ahn, J.H., Jiang, L., Shi, W., Son, S., Park, Y.J., Ryu, J.H., 2013a. Ocean color products from the Korean Geostationary Ocean Color Imager (GOCI). Opt. Express 21, 3835–3849.

Wang, M., Liu, X., Tan, L., Jiang, L., Son, S., Shi, W., Rausch, K., Voss, K., 2013b. Impact of VIIRS SDR performance on ocean color products. J. Geophys. Res. Atmos. 118, 10347–10360.

Wang, W.D., Robertson, R., Wang, Y., Zhao, C., Hao, Z.J., Yin, B.S., Xu, Z.H., 2022. Distinct Variability between Semidiurnal and Diurnal Internal Tides at the East China Sea Shelf. Remote Sens. 14, 2570. https://doi.org/10.3390/rs14112570.

Wang, M., Shi, W., 2007. The NIR-SWIR combined atmospheric correction approach for MODIS ocean color data processing. Opt. Express 15, 15722–15733.

Wang, M., Son, S., Harding, L.W., J.,, 2009. Retrieval of diffuse attenuation coefficient in the Chesapeake Bay and turbid ocean regions for satellite ocean color applications. J. Geophys. Res. 114, C10011. https://doi.org/10.1029/2009JC005286.

Wang, M., Shi, W., Jiang, L., 2012. Atmospheric correction using near-infrared bands for satellite ocean color data processing in the turbid western Pacific region. Opt. Express 20, 741–753.

Wang, M., Shi, W., Jiang, L., Voss, K., 2016. NIR- and SWIR-based on-orbit vicarious calibrations for satellite ocean color sensors. Opt. Express 24, 20437–20453.

Wang, M., Shi, W., Watanabe, S., 2020. Satellite-measured water properties in high altitude Lake Tahoe. Water Res. 178, 115839. https://doi.org/10.1016/j.watres.2020.115839.

Wu, J., Goes, J.I., do Rosario Gomes, H., Lee, Z., Noh, J.-H., Wei, J., Shang, Z., Salisbury, J., Mannino, A., Kim, W., Park, Y.-J., Ondrusek, M., Lance, V.P., Wang, M., Frouin, R., 2022. Estimates of diurnal and daily net primary productivity using the Geostationary Ocean Color Imager (GOCI) data. Remote Sens Environ 280, 113183. https://doi.org/10.1016/j.rse.2022.113183.

Yan, Y., Huang, K., Shao, D., Xu, Y., Gu, W., 2019. Monitoring the characteristics of the Bohai Sea ice using high-resolution geostationary ocean color imager (GOCI) data. Sustainability 11, 777. https://doi.org/10.3390/su11030777.

Yang, H., Choi, J.-K., Park, Y.-J., Han, H.-J., Ryu, J.-H., 2014. Application of the Geostationary Ocean Color Imager (GOCI) to estimates of ocean surface currents. J. Geophys. Res. Oceans 119 (6), 3988–4000.